



Reactive Collisions and Final State Analysis in Hypersonic Flight Regime 150005

Markus Meuwly
UNIVERSITÄT BASEL

09/13/2016
Final Report

DISTRIBUTION A: Distribution approved for public release.

Air Force Research Laboratory
AF Office Of Scientific Research (AFOSR)/ IOE
Arlington, Virginia 22203
Air Force Materiel Command

REPORT DOCUMENTATION PAGE				Form Approved OMB No. 0704-0188	
<p>The public reporting burden for this collection of information is estimated to average 1 hour per response, including the time for reviewing instructions, searching existing data sources, gathering and maintaining the data needed, and completing and reviewing the collection of information. Send comments regarding this burden estimate or any other aspect of this collection of information, including suggestions for reducing the burden, to Department of Defense, Executive Services, Directorate (0704-0188). Respondents should be aware that notwithstanding any other provision of law, no person shall be subject to any penalty for failing to comply with a collection of information if it does not display a currently valid OMB control number.</p> <p>PLEASE DO NOT RETURN YOUR FORM TO THE ABOVE ORGANIZATION.</p>					
1. REPORT DATE (DD-MM-YYYY) 13-09-2016		2. REPORT TYPE Final		3. DATES COVERED (From - To) 15 Oct 2014 to 14 Oct 2015	
4. TITLE AND SUBTITLE Reactive Collisions and Final State Analysis in Hypersonic Flight Regime				5a. CONTRACT NUMBER	
				5b. GRANT NUMBER FA9550-15-1-0005	
				5c. PROGRAM ELEMENT NUMBER 61102F	
6. AUTHOR(S) Markus Meuwly				5d. PROJECT NUMBER	
				5e. TASK NUMBER	
				5f. WORK UNIT NUMBER	
7. PERFORMING ORGANIZATION NAME(S) AND ADDRESS(ES) UNIVERSITÄT BASEL PETERSPLATZ 1 Basel, 4003 CH				8. PERFORMING ORGANIZATION REPORT NUMBER	
9. SPONSORING/MONITORING AGENCY NAME(S) AND ADDRESS(ES) EOARD Unit 4515 APO AE 09421-4515				10. SPONSOR/MONITOR'S ACRONYM(S) AFRL/AFOSR IOE	
				11. SPONSOR/MONITOR'S REPORT NUMBER(S) AFRL-AFOSR-UK-TR-2016-0028	
12. DISTRIBUTION/AVAILABILITY STATEMENT A DISTRIBUTION UNLIMITED: PB Public Release					
13. SUPPLEMENTARY NOTES					
14. ABSTRACT <p>Classical molecular dynamics simulations of the nonreactive collision between the N₂⁺ cation and Ar atoms at two different temperatures show that inelastic rotational excitation of the ion in the product channel is important and occurs more frequently than previously assumed. The simulations use an RKHS PES based on UCCSD(T)/aug-cc-pVTZ electronic structure calculations and correct handling of the asymptotics within the RKHS framework. Analysis of the results for j' = 6 using a strict filtering criterion of frac(v') = 0:001 and a figure-of-merit j* = 2 suggests that inelastic collisions occur in at least 17% of the cases, which is one order of magnitude larger than reported in earlier experiments (2%). Interestingly, the [N₂Ar]⁺ complex does not need to be formed (and stabilized) for rotational excitation to occur. A sufficiently close encounter of the two collision partners is sufficient to mutually influence their flight paths and lead to rotational excitation. It should be pointed out that the PES used in this work was calculated using a single-reference method. Electronic effects, which are not adequately captured using single-reference methods, might play a non-negligible role in the dissociative region of the PES. Consequently, further investigations should employ multi-reference methods such as MRCI to capture electronic effects which are, however, outside the scope of the present work. For a complete understanding of the rate of rotational excitation in the N₂⁺-Ar system, new experiments, which allow precise control of the exact quantum state of the collision partners and additional computational investigations at the quantum level are necessary.</p>					
15. SUBJECT TERMS EOARD, Hypersonic reactive flow					
16. SECURITY CLASSIFICATION OF:			17. LIMITATION OF ABSTRACT SAR	18. NUMBER OF PAGES 42	19a. NAME OF RESPONSIBLE PERSON CUMMINGS, RUSSELL
a. REPORT Unclassified	b. ABSTRACT Unclassified	c. THIS PAGE Unclassified			

				19b. TELEPHONE NUMBER <i>(Include area code)</i> 011-44-1895-616021
--	--	--	--	---

Reactive Collisions and Final State Analysis in Hypersonic Flight Regime

Computational Chemistry Group
Department of Chemistry
University of Basel
CH-4056 Basel

1 Overview

This report summarizes results obtained within the last Funding Period of the Project “Small-Molecule Reactions Relevant to the Hypersonic Flight Regime”. Part of the work has been published[1, 2] and other work is currently prepared for publication.[3]

2 Equilibrium Rate Coefficients from Atomistic Simulations: The $\text{O}(^3\text{P}) + \text{NO}(^2\Pi) \rightarrow \text{O}_2(X^3\Sigma_g^-) + \text{N}(^4\text{S})$ Reaction at Temperatures Relevant to the Hypersonic Flight Regime

Reactions involving nitrogen- and oxygen-containing small molecules occur in a wide range of processes. As an example, NO_2 - which can decay into $\text{NO} + \text{O}$ or $\text{O}_2 + \text{N}$ - plays a major role in atmospheric chemistry, as a smog constituent and in combustion processes.[4, 5, 6] The reaction characteristics changes from formation of NO_2 to exchange and dissociation reactions at higher temperatures (1000-20000 K). Above 20000 K, it is expected that the reactions will be dominated by the complete dissociation to the atomic species. In the hypersonic flight regime – which is the physical situation of interest in the present work – the chemistry will be in the intermediate case. Near the surface of such vehicles highly non-equilibrium conditions will be present with vibrational and rotational temperatures independently reaching several thousand Kelvin.[7] The gas-phase, surface reactions and energy transfer at these temperatures are essentially uncharacterized and the experimental methodologies capable of probing them are not well established. In this respect, theoretical and validated computational approaches become a valuable complement to experiments.

In order to model chemical kinetics under such non-equilibrium conditions, state- and temperature-dependent rate coefficients for individual reactions are required. However, direct experimentation under such conditions is usually not possible. In the present work, both forward and reverse reaction rate coefficients for $\text{O}(^3\text{P}) + \text{NO}(^2\Pi) \leftrightarrow \text{O}_2(X^3\Sigma_g^-) + \text{N}(^4\text{S})$ are calculated from molecular dynamics (MD) simulations for moderate to high temperatures (1000 to 20000 K) and compared with results from experimentally derived thermodynamics quantities from the NASA CEA (NASA Chemical Equilibrium with Applications) database.[8, 9] The value of such a validated computational approach is that it can be applied generically to a wide range of bimolecular reactions whenever direct experiments are not available, with consistency of the computations depending on a comparison of independent dynamic and energetic approaches.

A schematic representation of the relevant species for the $\text{O}(^3\text{P}) + \text{NO}(^2\Pi) \leftrightarrow \text{O}_2(^3\Sigma_g^-) + \text{N}(^2\text{P})$ reaction is given in Figure 1. NO_2 formation has a barrier of 1.3 eV from the $\text{N}+\text{O}_2$

side, whereas from the NO1+O2 side it is a barrierless process. In order to reach the N+O1O2 side from the NO1+O2 side, 2.6 eV are required including the barrier. An additional 5.6 eV are required for dissociation of O₂ and 6.9 eV for the dissociation of NO to the atomization state of N+O1+O2.

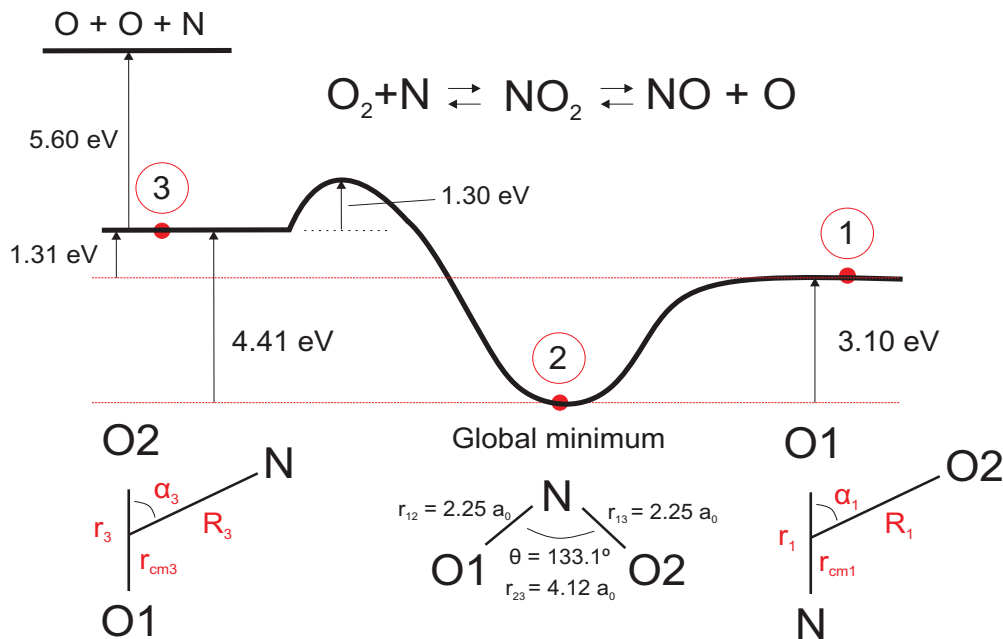


Figure 1: Relevant stages in the NO1+O2 reaction. The energies were derived from the *ab initio* calculations in Ref. [10].

Even when the excited states can approach the ground state PES for certain configurations (Figure 2), their influence can be considered to be minor. The first excited state is dissociative and about 6 eV are required to access the second and third excited states (see Figure 2). For the Maxwell-Boltzmann distribution at 20000 K, translational energies beyond 6 eV are accessed with little probability (0.06). This provides an upper bound since a thermal distribution requires additional energy to be distributed into rotational and vibrational motion. Furthermore, lifetimes of the system at the second and third excited states are presumably small since the wells are shallow. This causes the system to rapidly return to the ground state.[11] The expected effect of including electronically excited states is to somewhat lower the rate coefficients due to the topology of the excited PES (see Figure 2 which exhibits shallow minima that potentially stabilize intermediates for short times). Therefore, in this work we first consider only the ground state PES since it dominates the reaction dynamics under the relevant physicochemical conditions.

The equilibrium constant as a function of temperature for a chemical reaction at equilibrium is defined as,[12]

$$K(T) = \frac{k_+(T)}{k_-(T)}, \quad (1)$$

where $k_+(T)$ and $k_-(T)$ are the rate coefficients for the forward and reverse reactions, respec-

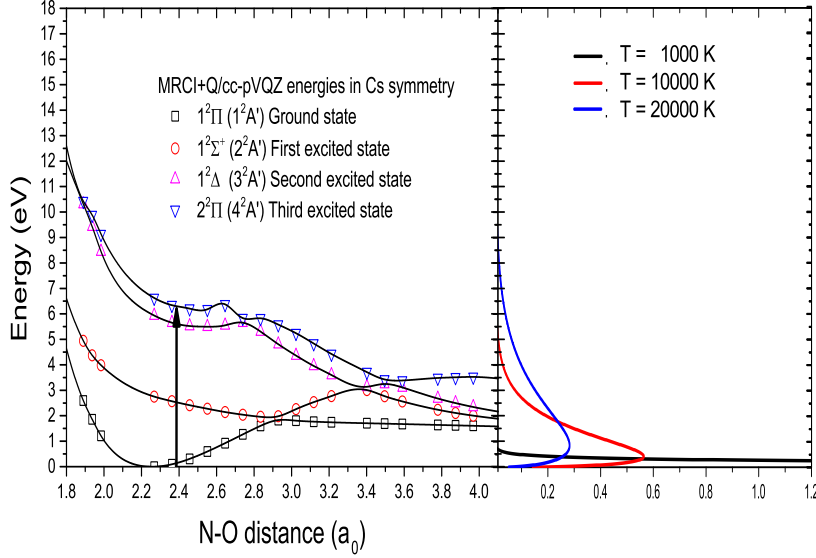


Figure 2: MRCI+Q/cc-pVQZ energies (symbols) for the O-NO coordinate with the other N-O distance fixed at $r_{\text{NO}} = 2.25 a_0$ for linear NO_2 arrangement. The solid lines are RKHS interpolants for each electronic state. The energy gap between the ground and third electronic state has been indicated by a vertical arrow. The panel on the right hand side reports the probability distribution function $P(E)$ for the total energy E .

tively. The rate coefficient for the forward reaction ($k_+(T)$) has been recently determined from atomistic simulations.[10] The same methodology is used here for the calculation of the rate coefficient for the reverse reaction $k_-(T)$. Following the previous work, three steps are involved: (1) the construction of the PES for the ground state of the NO_2 molecule based on high-level *ab initio* calculations and its representation with a reproducing kernel Hilbert space (RKHS) method[13] combined with Legendre polynomials; (2) quasi classical trajectory (QCT) calculations to study the adiabatic reaction dynamics, and (3) calculation of the rate coefficients for the different exit channels using an Importance Sampling Monte Carlo method.

The thermal rate coefficient from trajectory calculations is determined from[14]

$$k(T_t, T_{\text{rv}}, T_e) = \frac{\beta_t}{g(T_e)} \sqrt{\frac{8\beta_t}{\pi\mu}} \int_0^\infty \sigma(E_c; T_{\text{rv}}) E_c e^{-\beta_t E_c} dE_c, \quad (2)$$

where $\beta_t = k_B T_t$ and k_B is the Boltzmann constant, T_t , T_{rv} , T_e are the translational temperature of NO and O, the rovibrational temperature of NO and the electronic temperature of NO, respectively, $g(T_e)$ is the electronic degeneracy factor,[11, 15] μ is the reduced mass of NO and O, respectively, and $\sigma(E_c; T_{\text{rv}})$ is the integral cross section as a function of the collision energy, E_c and T_{rv} . In our studies it was assumed that $T_t = T_{\text{rv}} = T_e$. In other words, the various degrees of freedom in the reactants are in thermal equilibrium. If no subscript is shown for T then it corresponds to the common temperature. In a similar manner, the reaction cross section $\sigma(E_c; T_{\text{rv}})$ for a given collision energy E_c

$$\sigma(E_c; T_{\text{rv}}) = \frac{\sum_{v=0}^{v_{\text{max}}} \sum_{j=0}^{j_{\text{max}}(v)} (2j+1) e^{-\beta_{\text{rv}} E_{vj}} \sigma_{vj}(E_c; vj)}{\sum_{v=0}^{v_{\text{max}}} \sum_{j=0}^{j_{\text{max}}(v)} (2j+1) e^{-\beta_{\text{rv}} E_{vj}}}, \quad (3)$$

where $\sigma_{vj}(E_c)$ is the (v, j) -state dependent cross section at collision energy E_c . The energy E_{vj} of a rovibrational state (v, j) is calculated according to a Morse oscillator model for the NO molecule.[16] The cross section as an integral of the opacity function $P_{vj}(b; E_c)$ for given E_c and rovibrational state (v, j) is

$$\sigma_{vj}(E_c) = \int_0^{\infty} P_{vj}(b; E_c) 2\pi b db \quad (4)$$

The integral in Eq. 2 can be calculated by using an Importance Sampling Monte Carlo scheme.[17] For this, the vibrational and rotational quantum numbers v and j , and the collision energy (E_c) are sampled from the Boltzmann-weighted probability distribution function

$$p_{vj}(T_{\text{rv}}) = \frac{(2j+1) e^{-\beta_{\text{rv}} E_{vj}}}{\sum_{v'=0}^{v_{\text{max}}} \sum_{j'=0}^{j_{\text{max}}(v')} (2j'+1) e^{-\beta_{\text{rv}} E_{v'j'}}}, \quad (5)$$

and

$$\rho(E_c) dE_c = \beta_{\text{t}}^2 E_c e^{-\beta_{\text{t}} E_c} dE_c, \quad (6)$$

respectively.

For the determination of the upper limit (b_{max}) of the relevant sampling interval for the impact parameter, b , preliminary tests were carried out at low temperatures (100 and 200 K). As NO_2 was not formed for $b \geq 26 \text{ a}_0$, the impact parameter was therefore uniformly sampled from 0 up to $b_{\text{max}} = 26 \text{ a}_0$. As the opacity curves in Figure 3 show, this upper limit is very conservative and ensures convergence of the results with respect to b . However, large b is required for low-energy collisions.[10]

After evaluating the integral in Eq. 2 over v , j and E_c , the resulting expression for $k(T)$ is

$$k(T) = \sqrt{\frac{8}{\pi \mu \beta}} \frac{2\pi b_{\text{max}}}{g(T) N_{\text{tot}}} \sum_{i=1}^{N_{\text{reac}}} b_i, \quad (7)$$

where N_{reac} and N_{tot} are the number of reactive and the total number of trajectories, respectively, and b_i is the impact parameter of reactive trajectory i . The convergence of the integral in Eq. 2 was monitored by the decrease of the Monte Carlo error.[10] Choosing eigenenergies from a Morse-oscillator for the NO molecule was done for convenience. To quantify the expected difference in using a kernel-interpolated 1-dimensional potential for the NO oscillator, the bound states from the Morse-fit and the RKHS were determined up to $v = 6$ (corresponding to $\approx 12000 \text{ cm}^{-1}$). The correlation between the two sets of eigenenergies is better than

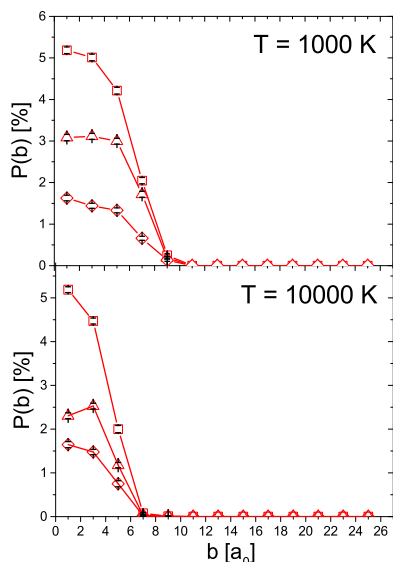


Figure 3: Thermal opacity functions for 1000 and 10000 K on the upper and lower panels, respectively. The calculated points for NO₂ formation in the high pressure limit (open squares), oxygen exchange channel (triangles) and the "O1O2+N" channel (open diamonds) have been represented. Error bars are indicated in black.

0.999 with a slope of 1.0003. Hence, over the relevant energy range the initial conditions from a Morse-oscillator model are expected to closely reflect those from using the more accurate kernel-interpolated potential.

The rate coefficients for the reverse ($k_-(T)$) and forward reaction ($k_+(T)$) derived directly from trajectory calculations[10] in the present work are reported in Figure 4 for temperatures between 300 and 20000 K. An inset with results for the range from 1000 to 5000 K has also been included. The curve from this work represents a fit to a modified Arrhenius equation (see Eq. 8).[18] A total of 10000 trajectories was run for the NO+O reaction whereas only 5000 were necessary for the reverse reaction to obtain a rate coefficient with a relative error of better than 10 %. It is found that a directly measured data point at 3000 K (green star) agrees very favorably with the atomistic simulations (magenta) for $k_+(T)$. [10]

$$k(T) = AT^n e^{-E_a/T}, \quad (8)$$

where A is the pre-exponential factor and E_a is the activation energy. The parameters resulting from the fit are $A = 9.35 \times 10^8 \text{ cm}^3\text{s}^{-1}\text{mol}^{-1}\text{K}^{-n}$, $E_a = 1.88 \times 10^4 \text{ kcal/mol}$ and $n = 0.93$.

Forward rate coefficients ($k_+(T)$) have been reported in previous works most of which were based on computation. Valli *et al* reported $k_+(T)$ from quasi classical trajectory calculations using the ground state PES of the NO₂ molecule for temperatures ranging from 300 to 500 K.[19] This data has been extended to higher temperatures by means of a fit to Eq. 8. The resulting parameters are $A = 1.65 \times 10^{13} \text{ cm}^3\text{s}^{-1}\text{mol}^{-1}\text{K}^{-n}$, $E_a = 2.13 \times 10^4 \text{ kcal/mol}$ and $n = 0$. In the review of reactions relevant to Combustion Chemistry by Baulch *et al.* $k_+(T)$

for temperatures ranging from 1000 to 5000 K are reported and fit to Eq. 8 with parameters $A = 6.87 \times 10^8 \text{ cm}^3\text{s}^{-1}\text{mol}^{-1}\text{K}^{-n}$, $E_a = 1.9 \times 10^4 \text{ kcal/mol}$ and $n = 1.13$. [20]

Bose *et al* reported rate coefficients for the reverse reaction ($k_-(T)$) based on QCT on the $^2A'$ and $^4A'$ PESs for temperatures ranging from 1000-14000 K. [21] In order to obtain the forward reaction rate coefficients using Eq.1, these data were combined with CEA data [8, 9] for the equilibrium rates ($K(T)$) (available from 300-20000 K). These results were extended over the whole range of temperatures from 300-20000 K by fitting Eq.8 which yielded the following parameters $A = 2.49 \times 10^9 \text{ cm}^3\text{s}^{-1}\text{mol}^{-1}\text{K}^{-n}$, $E_a = 0.4 \times 10^4 \text{ kcal/mol}$ and $n = 1.18$.

At lower temperatures (below 1000 K) experimental data is available for k_+ which compares very favourably with the computed values as well. At sufficiently low temperatures quantum effects (effect of zero point energy and tunneling) will become important. A recent study of the proton transfer reaction in malonaldehyde has established that zero point effects can play an important role whereas tunneling probably only becomes important at the lowest temperatures. [22] However, this temperature range is not of primary importance for the present work.

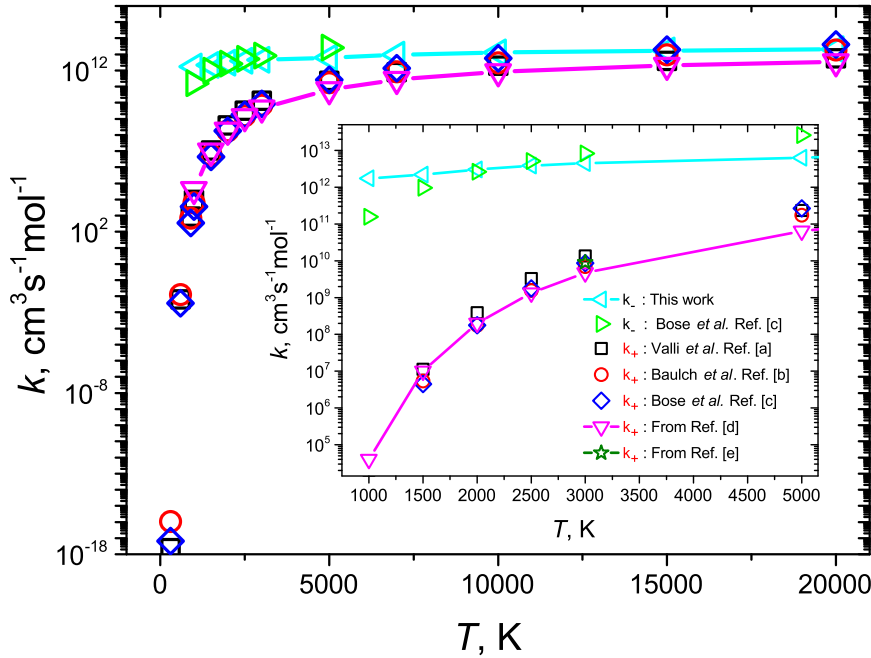


Figure 4: Rate coefficients $k_-(T)$ (blue open triangles) and $k_+(T)$ (red open triangles) for temperatures between 300 and 20000 K. An inset with results for the range from 1000 to 5000 K has been included. In the legend [a]=Ref.[19], [b]=Ref.[20], [c]=Ref.[21], [d]=Ref.[10] and [e]=Ref.[23].

The equilibrium rates from the present work obtained directly from the trajectory calculations are compared to the equilibrium constants calculated from the CEA database [8, 9, 24]

in Figure 5 for temperatures between 5000 and 20000 K. For temperatures below 6000 K, the CEA functions are fit to available experimental data whereas above 6000 K, the CEA results have been obtained from usual statistical thermodynamic expressions for equilibrium rates, based on spectroscopic constants of the atoms and molecules involved. The results in Figure 5 show that CEA equilibrium constants are somewhat underestimated for temperatures below 10000 K and agree almost quantitatively for higher temperatures.

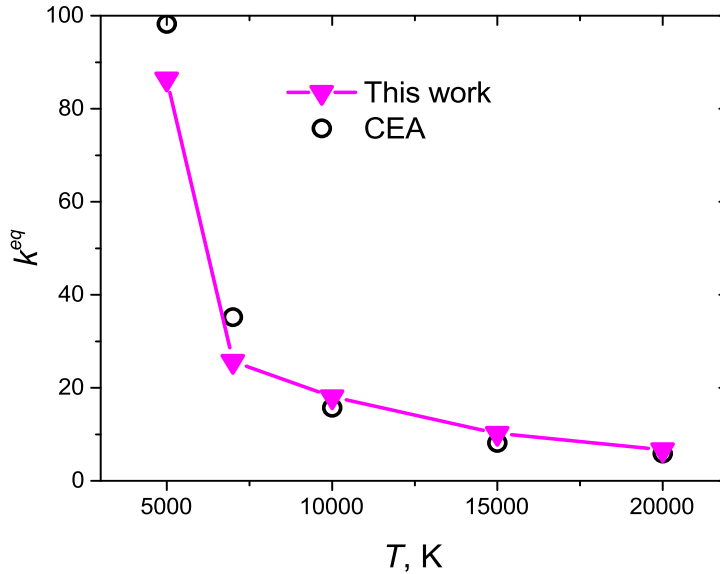


Figure 5: Equilibrium rate coefficients $K(T)$ for temperatures between 5000 and 20000 K. Results from CEA are also included for comparison.[8, 9]

In conclusion, the equilibrium rate coefficient for the $O(^3P) + NO(^2\Pi) \leftrightarrow O_2(X^3\Sigma_g^-) + N(^4S)$ reaction was calculated directly from molecular dynamics simulations on accurate PESs fitted to high-level electronic structure calculations. The $K(T)$ thus obtained compare favorably with experimental measurements from CEA over a wide temperature range extending up to 20000 K.[8, 9, 24] The influence of higher electronic states for higher temperature is minor. The forward rate coefficients from this work have been validated against theoretical results from previous works.[19, 20, 21] and the present ansatz provides a generic computational framework for obtaining such data from computation.

3 Reaction Dynamics for the $N(^4S) + NO(^2\Pi)$ System at Temperatures Relevant to the Hypersonic Flight Regime

Nitric oxide (NO) plays a major role in the chemistry near the surface of vehicles for atmospheric re-entry in the hypersonic flight regime [25]. Therefore, reactions of nitric oxide with the most common atmospheric gases, e.g. N and O, must be considered in the design of spacecraft. Modelling the thermochemical phenomenon in the re-entry flows requires the

knowledge of rate coefficients of such reactions at very high temperatures. At such extreme conditions quantitative experiments are difficult and expensive. Consequently, computational studies are vital for characterizing the reactivity or energy transfer in reactive or nonreactive encounters of such systems.

Recently, a study of NO formation in hypersonic boundary layers[25] around space vehicles during re-entry showed that the inclusion of the NO data in the models modified the mass fraction and the heat flux substantially in the boundary layers. The ground state of N_2O has been studied intensely both, theoretically and experimentally.[26, 27, 28, 29, 30, 31, 32, 33, 34] However, the potential energy surfaces (PESs) that connect $\text{NO}(X^2\Pi)+\text{N}(^4S)$ with $\text{N}_2(X^1\Sigma)+\text{O}(^3P)$ are in the triplet manifold, see Figure 6. Several experimental studies of the $\text{NO}(X^2\Pi)+\text{N}(^4S)\rightarrow\text{N}_2(X^1\Sigma)+\text{O}(^3P)$ reaction have been performed over the past decades [35, 36, 34, 37, 38, 39] Nevertheless, the agreement between the experimental results is poor, e.g. at 100 K Fox[40] derived a rate of $3.60\times 10^{-13}\text{ cm}^3\text{molecule}^{-1}\text{s}^{-1}$ while Bergeat *et al* [41] report a value of $4.11\times 10^{-11}\text{ cm}^3\text{molecule}^{-1}\text{s}^{-1}$.

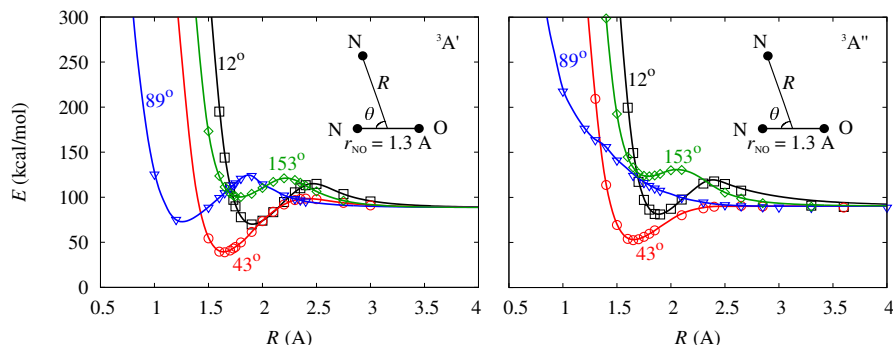


Figure 6: Schematic representation of the $C_{\infty v}$ and C_s (NON -angle near 130°) partial adiabatic correlation diagrams for N_2O . Data taken from Ref. [42]. The Boltzmann distribution at 1000 K (red line) and 10000 K (blue line) for the initial $\text{NO}(X^2\Pi)$ are represented together with the lowest vibrational states.

Theoretical studies of the scattering on the adiabatic electronic states have been done on the $^3A'$ and $^3A''$ surfaces.[43, 44, 45, 46] The PESs of Garmallo *et al* [45] have been considered up recently as the best reported in the literature [25]. The analytical representation of these surfaces is based on a many-body expansion derived from a grid of *ab-initio* data computed with the CASPT2 method. Very recently, new PESs for the two lowest triplet states were published.[47] These surfaces were calculated at the multi reference configuration interaction (MRCI) level and showed remarkable differences compared to the PESs of Garmallo *et al* [45]. The global minimum of the $^3A''$ was found to be 0.23 eV deeper than in the previous work. For the $^3A'$ state several new minima and transition states were found. Therefore, MRCI calculations are required for computing meaningful rates.

The new available PESs[47] are limited to study the $\text{N}_2+\text{O}\rightarrow\text{NO}+\text{N}$ forward reaction. This is due to the R^{-6} dependence in the long range (dispersion and induction interaction) is not included explicitly in the fit. The N_2+O reaction is highly endothermic, and the dynamics in this direction is very expensive computationally. Very recently, the same group presented a

quasiclassical trajectory study of the $\text{N}_2+\text{O}\rightarrow\text{NO}+\text{N}$ using their surfaces [48]. In that work, they concluded that the reaction occurs predominantly in the $^3\text{A}''$ surface. However, no rate coefficients necessary in the models of the atmospheric re-entry were determined.

In the present work new PESs for the $^3\text{A}'$ and $^3\text{A}''$ states of N_2O are presented. These PESs are used to study the $\text{NO}(X^2\Pi)+\text{N}(^4\text{S})$ collision and computed the thermal rate coefficients at high temperatures. In the next section, the methods used in the development of the PESs are described, and also a brief description scattering calculations is included. The results are discussed in Section III, while the main conclusions are in Section IV.

3.1 Methods

Ab-initio calculations

The *ab-initio* potential energies of the triplet states of N_2O were computed at the multireference configuration interaction (MRCI) level including the Davidson correction (MRCI+Q), [49] preceded by complete active space self-consistent field (CASSCF) calculations. The standard Dunning's correlation consistent polarized triplet-zeta (cc-pVTZ) basis set [50] were used. Also, a set of points was computed using the coupled cluster method with single and double electronic excitations and perturbative treatment of triple excitation (CCSD(T)) for ascertaining the quality of the MRCI+Q calculations in the long range part ($R \rightarrow \infty$). All electronic structure calculations were performed with the Molpro package [51].

In both electronic states, $^3\text{A}'$ and $^3\text{A}''$, the asymptotic N_2+O and $\text{NO}+\text{N}$ channels were treated separately. In each case, energies on a three-dimensional grid for the respective Jacobi coordinates (R , r and θ) were computed. For N_2+O , the angles vary between 0° and 90° . The angular interval was extended up to 180° , taking into account the symmetry of the system. In this way, the number of angular points is the same that for $\text{NO}+\text{N}$, which is necessary for the fitting. In total, 11 angular points were taken into account in each channel. MRCI+Q calculations for the $^3\text{A}'$ state of the N_2+O asymptote were carried out for 19 distances along R ($R \in [1.1, 10.0]$ Å), and 13 points along r ($r \in [0.90, 1.47]$ Å) whereas for the $\text{NO}+\text{N}$ asymptote they included $R \in [1.0, 10.0]$ Å and $r \in [0.90, 1.55]$ Å. For the $^3\text{A}''$ state the same R intervals were used whereas for the N_2+O channel $r \in [0.90, 1.55]$ Å and $r \in [0.90, 1.58]$ Å for the $\text{NO}+\text{N}$ channel.

Representation of the PESs

All PESs were represented by using a reproducing kernel Hilbert space approach (RKHS). [52] The potential energy for each channel is

$$V(\mathbf{x}) = \sum_{k=1}^M \alpha_k Q(\mathbf{x}_k, \mathbf{x}) \quad (9)$$

where M is the number of *ab-initio* points, \mathbf{x} is the vector of the internal coordinates $\mathbf{x} = (R, r, z)$, with $z = \frac{(1-\cos\theta)}{2}$, and \mathbf{x}_k corresponds to a grid point $\mathbf{x}_k = (R_k, r_k, z_k)$. $Q(\mathbf{x}_k, \mathbf{x})$ is the reproducing kernel for a multidimensional PES, which corresponds to the multiplication of three 1-dimensional reproducing kernels

$$Q(\mathbf{x}_k, \mathbf{x}) = q^{2,6}(R_k, R) q^{2,6}(r_k, r) q^2(z_k, z) \quad (10)$$

The coefficients α_k are determined from solving the linear system

$$\begin{pmatrix} Q(\mathbf{x}_1, \mathbf{x}_1) & Q(\mathbf{x}_1, \mathbf{x}_2) & \cdots & Q(\mathbf{x}_1, \mathbf{x}_M) \\ Q(\mathbf{x}_2, \mathbf{x}_1) & Q(\mathbf{x}_2, \mathbf{x}_2) & \cdots & Q(\mathbf{x}_2, \mathbf{x}_M) \\ \vdots & \vdots & \ddots & \vdots \\ Q(\mathbf{x}_M, \mathbf{x}_1) & Q(\mathbf{x}_M, \mathbf{x}_2) & \cdots & Q(\mathbf{x}_M, \mathbf{x}_M) \end{pmatrix} \begin{pmatrix} \alpha_1 \\ \alpha_2 \\ \vdots \\ \alpha_M \end{pmatrix} = \begin{pmatrix} V(\mathbf{x}_1) \\ V(\mathbf{x}_2) \\ \vdots \\ V(\mathbf{x}_M) \end{pmatrix} \quad (11)$$

By construction, reproducing kernels decay to zero for $R \rightarrow \infty$. Hence, for having a correct representation of the asymptotic behaviour of the kernel interpolation, the energy at large atom-diatom distance $V(R \rightarrow \infty, r, \theta)$ was subtracted from the values of the grid, such that each cut $V^{\text{cut}}(R, r, \theta)$ dissociates to zero. The potential $V^{\text{cut}}(R, r, \theta)$ is then represented as an RKHS. The asymptotic energies $V(R \rightarrow \infty, r, \theta)$, considered isotropic, are also fitted using a 1-dimensional kernel. The total energy is the sum of the energies of both interpolations $V(R, r, \theta) = V^{\text{cut}}(R, r, \theta) + V(R \rightarrow \infty, r, \theta)$. The procedure is similar to that used for $\text{Ar} + \text{N}_2^+$ [2].

The reactive PES was constructed by smoothly connecting the three PESs (AB+C, AC+B, and BC+A), each represented as a RKHS (Eq. 9) with a distance-dependent switching function, as was previously done for NO_2 . [53, 1] The global PES is therefore

$$V(\mathbf{y}) = \sum_{i=1}^3 w_i(\mathbf{y}) V_i(\mathbf{y}) \quad (12)$$

where the \mathbf{y} is the vector of the three inter-atomic distances of the N_2O molecule, and V_i are the potential energies of the three asymptotic PESs. The switching function is

$$w_i(y_i) = \frac{e^{-(y_i/a)^4}}{\sum_{j=1}^3 e^{-(y_j/a)^4}} \quad (13)$$

where y_i are either of the inter-atomic distance and the parameter a was set to 1.0 for the $^3\text{A}'$ PES and 1.2 in the $^3\text{A}''$ surface. This parameter determines the range over which the PESs are mixed.

Furthermore, an independent grid of points was computed for describing the diatomic molecules N_2 and NO , using the same method that in the calculation of the global PES. These points were fitted to the Morse potential function using a least squares procedure. Table 1 summarizes the properties of both molecules. The dissociation energy is lower than the experimental data, however, this should not affect the calculations as the full dissociation of N_2O into $\text{N} + \text{N} + \text{O}$ is not considered here. These Morse parameters are then used for generating initial conditions for the quasiclassical trajectories (QCT) studies.

Table 1: Morse parameters and diatomic data of N₂ and NO.

	r_e (Å)	D_e (eV)	β (Å ⁻¹)	ω_e (cm ⁻¹)	$\omega_e x_e$ (cm ⁻¹)
N ₂					
calc.	1.105	9.385	2.799	2389.579	18.858
expt.	1.098	9.905		2358.570	14.324
NO					
calc.	1.158	6.234	2.942	1982.032	19.532
expt.	1.151	6.614		1904.200	14.075
Experimental values from Ref. [54].					

QCT calculations

Quasiclassical trajectory calculations are used to determine thermal rates coefficients from

$$k(T_t, T_v, T_r, T_e) = \sqrt{\frac{8\beta_t^3}{\pi\mu}} \int_0^\infty \sigma(E_c; T_t; T_v) E_c e^{-\beta_t E_c} dE_c \quad (14)$$

where T_t , T_v , T_r and T_e are the translational, vibrational, rotational and electronic temperature, $\beta_i = 1/(k_B T_i)$, i denotes the respective temperature, E_c is the collisional energy, and k_B is the Boltzmann constant. The various degrees of freedom in the reactants are considered to be in thermal equilibrium, i.e. $T_t = T_v = T_r = T_e$ and it will be referred to as T for the remainder of the work. The cross section $\sigma(E_c; T)$ (using $T = T_v = T_r = T_e$) is defined by

$$\sigma(E_c; T) = \sum_{\nu=0}^{\nu_{\max}} \sum_{j=0}^{j_{\max}(\nu)} \frac{(2j+1)e^{-\beta E_{\nu j}}}{Q_{rv}} \sigma(E_c; \nu, j) \quad (15)$$

where Q_{rv} is the rovibrational partition functions, ν and j are the vibrational and rotational quantum numbers, and $E_{\nu j}$ is the respective internal energy in the ν and j state. The state-to-state cross section is

$$\sigma(E_c; \nu, j) = 2\pi \int_0^\infty P_{\nu j}(b; E_t) b db \quad (16)$$

where $P_{\nu j}(b; E_t)$ is the opacity function, and b the impact parameter.

The dynamics of the system is followed by propagating the equations of motions for a given set of initial conditions. These equations were integrated numerically using the Velocity-Verlet algorithm [55]. The initial conditions for NO were generated from a WKB-quantized periodic orbit[56] of the corresponding rotating Morse oscillator for a given ν and j [57]. The symmetry axis of NO, the axis of its rotation, and the angular momentum were randomly oriented and the integral Eq. 14 was evaluated using an Importance Sampling Monte Carlo scheme.[58] The rotational and vibrational quantum numbers and the collision energy E_c were sampled using the probability distributions

$$p_{\nu j}(T) = \frac{(2j+1)e^{(-\beta E_{\nu j})}}{\sum_{\nu'=0}^{\nu_{\max}} \sum_{j'=0}^{j_{\max}(\nu')} (2j'+1)e^{-\beta E_{\nu' j'}}} \quad (17)$$

and

$$\rho(E_c)dE_c = \beta^2 E_c e^{-\beta E_c} dE_c \quad (18)$$

The impact parameter was sampled from 0 to b_{\max} using an Importance Sampling Monte Carlo scheme from which the rate coefficient is determined as

$$k(T) = g_e(T) \sqrt{\frac{8}{\mu\pi\beta}} \frac{2\pi b_{\max}}{N_{\text{tot}}} \sum_{k=1}^{N_{\text{reac}}} b_k \quad (19)$$

where N_{tot} and N_{reac} are the total and the reactive number of trajectories, respectively, and b_k is the impact parameter of reactive trajectory k . This last equation includes the electronic degeneracy factor g_e , which is defined as

$$g_e(T) = q_{\text{N}_2\text{O}}(T) q_{\text{N}(^4\text{S})}^{-1}(T) q_{\text{NO}(^2\Pi)}^{-1}(T) \quad (20)$$

where the electronic partition functions are $q_{\text{N}_2\text{O}} = 3$ (for both states $1^3\text{A}'$ and $1^3\text{A}''$), $q_{\text{N}(^4\text{S})} = 4$ and $q_{\text{NO}(^2\Pi)}(T) = 2 + 2\exp(-177.1/T)$.

Overall, 10000 trajectories at nine temperatures between 100 K and 20000 K were computed. For each temperature, conservation of the total energy was verified. A time step of 0.01 fs was used, and the maximum impact parameter was set large enough that only elastic collisions take place ($b_{\max} = 10.05$ Å and 9.58 Å for the $^3\text{A}'$ and $^3\text{A}''$ respectively). For several T , a second set of calculations was run with a small value of b_{\max} for having a sufficient number of trajectories to analyse the exchange channel. The final rate coefficients were calculated from the values determined in the calculation on each PES,

$$k(T) = k_p(T) + k_{\text{pp}}(T) \quad (21)$$

where k_p and k_{pp} are the rate coefficients from simulations on the $^3\text{A}'$ and $^3\text{A}''$ PES, respectively.

3.2 Results

Quality of the Potential Energy Surfaces

The quality of the RKHS PESs is reported in Figure 7. The cusp regions due to the surface crossing regions, which were one of the main causes of errors in earlier PESs [47], are treated satisfactorily. The pronounced angular dependence of the energy as a function of R , also is shown in this figure for a typical cut at $r_{\text{NO}} = 1.3$ Å.

The experimental relative energies of the different channels can be compared with the analytical PESs. These data are summarized in Table 2. The surfaces developed in this work underestimate the relative experimental reaction energy ($\text{NO} + \text{N} \rightarrow \text{N}_2 + \text{O}$) by less than 3.6% while for the full atomization this value reduces up to 1.5%. Li *et al* [26] used an extrapolation procedure for matching the energies of the reactant and products to the experimental ones which is empirical and probably not valid globally. Therefore, we decided not to include any semi-empirical parameter. The approach used in this study is geared towards probing the performance of a given level of theory which can eventually be improved by morphing procedures [59] together with experimental data (e.g. from spectroscopy; reactive scattering,

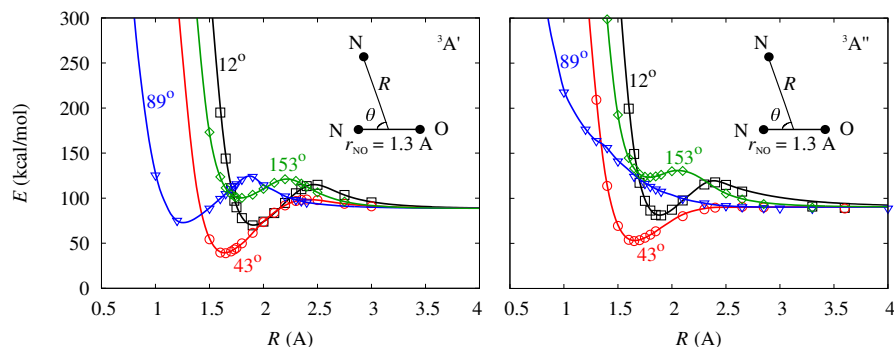


Figure 7: One-dimensional potential energy curves for the NO+N grid at $r_{\text{NO}} = 1.3 \text{ \AA}$ for several values of θ and the $^3A'$ (left) and $^3A''$ (right) states. The lines are the RKHS-energies and the points correspond to the *ab-initio* energies.

Table 2: Reaction energies from the PESs developed in this work and the corresponding experimental data (in kcal/mol).

reaction	$^3A'$	$^3A''$	exp ^a
NO+N→N+N+O	154.89	154.92	152.60
N ₂ +O→N+N+O	228.02	228.01	228.40
N ₂ +O→NO+N	73.12	73.09	75.80

^a Experimental values from [47] taken from [60]

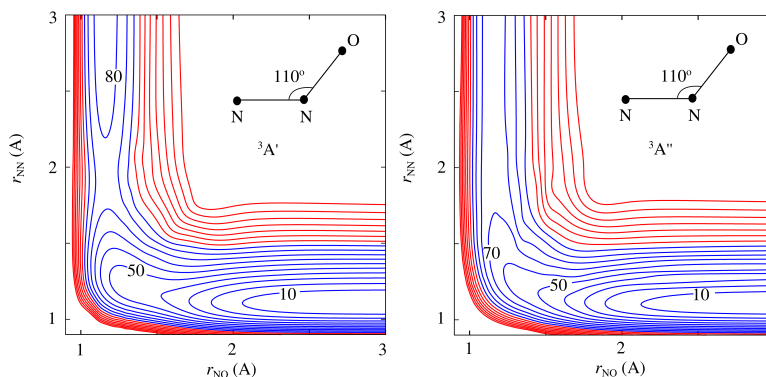


Figure 8: Contour plots at the NNO angle of 110° . Contour are incremented in step of 10 kcal/mol (blue lines are used for $E \leq 100$ kcal/mol and red line for $E > 100$ kcal/mol). The zero of energy correspond to the valley of the N₂+O asymptotic PES.

etc.).

The NO+N \rightarrow N₂+O is a direct reaction only on the the $^3A''$ surface as can be seen in Figure 8. Other contour-plot at $r_{\text{NO}} = 1.15 \text{ \AA}$ is represented in Figure 9 for the $^3A''$ state. These plots also show the smoothness typical of the kernel interpolations.

The $^3A'$ surface is more complex than the $^3A''$ one. In this case, almost all the minima and transition states have an N-O distance close to 1.3 \AA . Therefore, the contour plot at $r_{\text{NO}} = 1.3 \text{ \AA}$ is reported in Figure 10. Similar topography was shown in Figure 9 of Ref. [47].

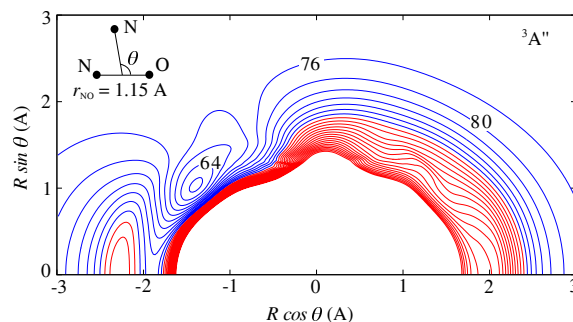


Figure 9: Potential energy surface for NO+N at a fix diatomic distance $r_{\text{NO}} = 1.15 \text{ \AA}$ for the $^3A''$ state. Isocontours are shown in increments of 4 kcal/mol (blue lines are used for $E \leq 100$ kcal/mol and red line for $E > 100$ kcal/mol). The zero of energy correspond to the valley of the N_2+O asymptotic PES. In this graphics, the linear NON corresponds to a Jacobi angle of zero degree

This agreement with Ref. [47] was expected as the *ab-initio* calculations in both studies were done at the MRCI level, even though in the present study the energies was computed using a cc-pvtz basis set and represented with a RKHS method while Lin *et al* employed the maug-cc-pVTZ and a fitting function formed by a sum of pairwise term and permutationally invariant polynomials in bond orders. The main difference is that the PESs of the present work can be employed to study both, NO+N collisions (including atom exchange) and N_2 formation for the N_2+O channel. The long range part of the potential is described by the $q^{2,6}(R_k, R)$ kernel which gives the correct behavior of the dispersion and induction interactions (R^{-6}) for large R .

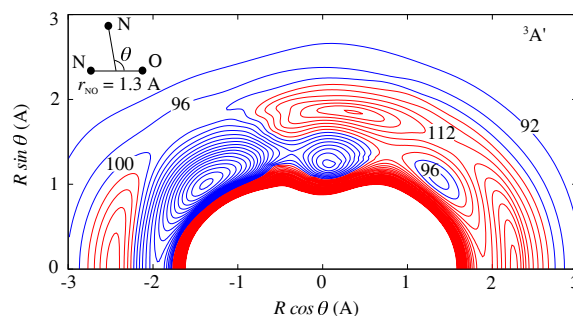


Figure 10: Potential energy surface for NO+N at the $^3A'$ state with r_{NO} fixes at 1.3 \AA . At this diatomic distance almost all stationary points can be seen. Contour are incremented in step of 4 kcal/mol (blue lines are used for $E \leq 100$ kcal/mol and red line for $E > 100$ kcal/mol). The zero of energy correspond to the valley of the N_2+O asymptotic PES. In this graphics, the linear NON corresponds to a Jacobi angle of zero degree.

Dynamics

The PESs were used to follow the different reaction channels over temperatures ranging from 100 K to 20000 K. Figure 11 shows the distribution of probabilities of the rovibrational energy, vibrational and rotational quantum number at 5000 K for both products, NO and N_2 ,

separately. It can be seen that formation of N_2 with low rovibrational energies is allowed on the $^3A''$ state but not for $^3A'$ at 5000 K. Consequently, small vibrational quantum numbers are less probable in the $^3A'$ PES. The $^3A''$ surface allows direct reactions and N_2 can finish in the ground vibrational state. N_2 formation on the $^3A'$ PES involves several stationary points of the surface, allowing more efficient redistribution of energy in the very small number of trajectories (32) that lead to N_2 . Alternatively, the atom exchange reaction ($N^1O+N^2 \rightarrow N^2O+N^1$) on the $^3A'$ and $^3A''$ surface is improbable and occurs only for 0.3 % and 0.7 % of the trajectories at 5000 K. Therefore, their contribution to the final distributions of NO is very small and the $N^1O+N^2 \rightarrow N^1O+N^2$ is the predominant process in both surface. In this case, the $\Delta\nu = 0$ are the most favoured transitions with a probability of 89% in the $^3A'$ state and 82% on the $^3A''$ surface. Also the averaged final vibrational energy of the products (NO and N_2), defined as $\langle E_\nu \rangle = \sum_i p(\nu_i) E_\nu^i$, are represented.

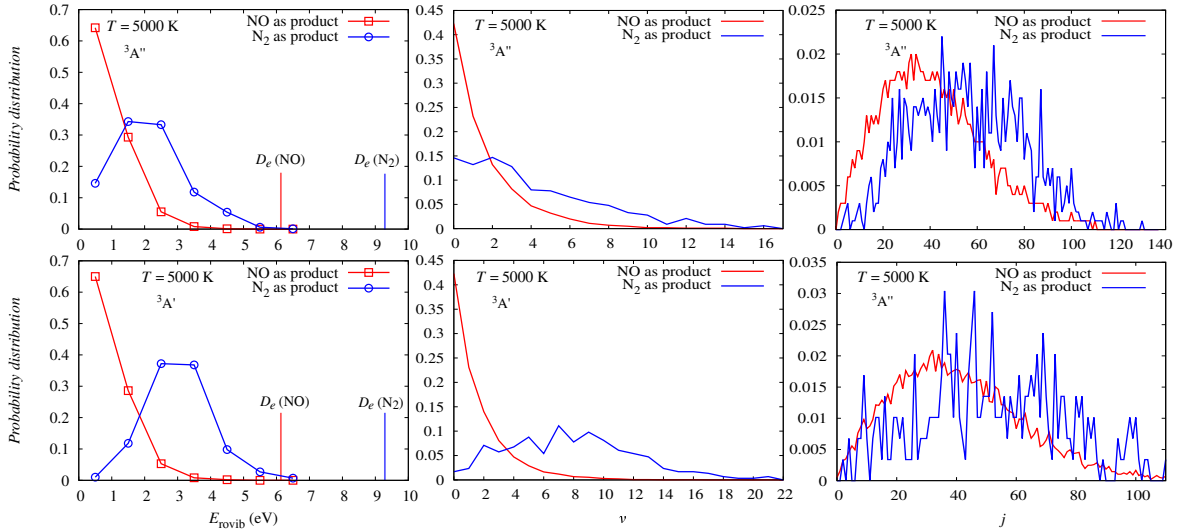


Figure 11: Rovibrational distribution at $T = 5000$ K.

Figure 12 reports the probability distributions of the rovibrational energies together with the vibrational and rotational quantum number for simulations at $T = 20000$ K. Rovibrational states with energies larger than the dissociation energy of the diatomic systems were found. At this temperature, high rotational states are populated and the effective potential, which includes the centrifugal barrier ($V^{\text{eff}}(r) = V(r) + \frac{j(j+1)}{2\mu r^2}$), prevents dissociation. Also, full atomization of the system is possible but only a few trajectories finished in this channel. As this channel is not of particular interest to this work it was not further considered. The probability of the $N^1O+N^2 \rightarrow N^2O+N^1$ channel at 20000 K is 3.1% in the $^3A'$ state and 4.7% for the $^3A''$. These values show a pronounced dependence on T when compared with the respective probabilities ($\leq 0.7\%$) at 5000 K. The barrier in the surfaces for the $N^1O+N^2 \rightarrow N^2O+N^1$ reaction make this channel significant only at high temperatures. Figure 12 also shows the distribution of NO due to the $N^1O+N^2 \rightarrow N^1O+N^2$ and $N^1O+N^2 \rightarrow N^2O+N^1$ channels. If no rearrangement occurs during the collision, the rotational distributions have a Boltzmann behavior. However, the formation of N_2 and the exchange of nitrogen do not show clearly a Boltzmann distribution. Therefore, assuming one temperature for the products

could not be a good approximation.

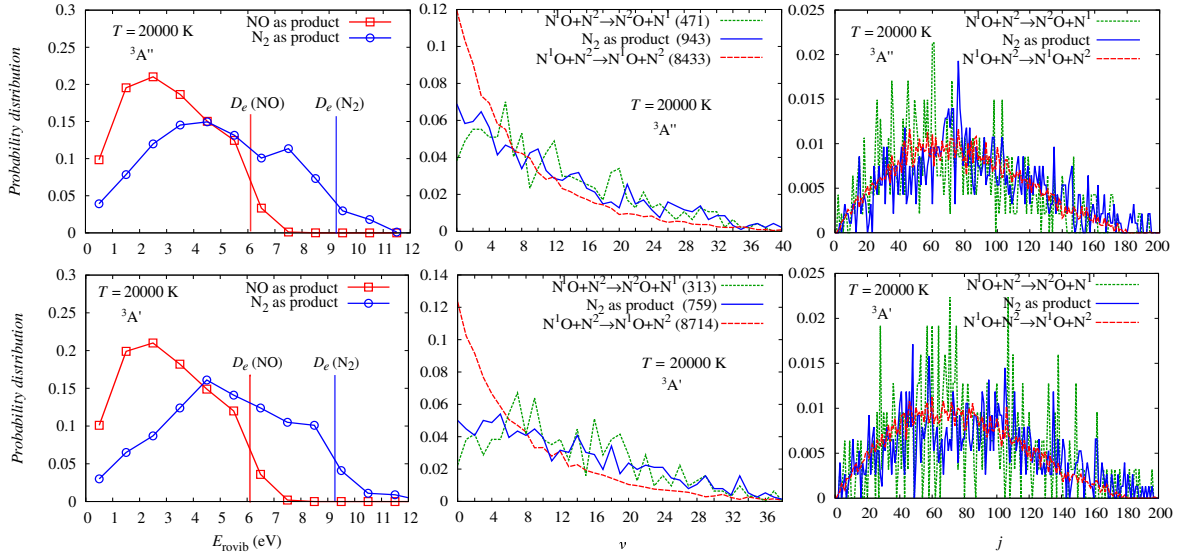


Figure 12: Rovibrational distribution at $T = 20000$ K. In parenthesis the number of trajectories that finish in each channel.

An exploratory set of time-independent (TI) quantum reactive scattering calculations were performed using both PESs. The *abc* code [61] was used for studying the NO+N collision at several total energies E_t . This code solves the time-independent Schrödinger equation of a triatomic system using the coupled-channel hyperspherical coordinate method. The calculations were performed for total angular momentum $J = 0$. After some convergence tests, the maximum value of j included in any channel was 50, and the maximum internal energy was set to 4.0 eV. The value of maximum hyperradius ρ_{\max} was fixed to 20 a_0 and 400 step in the log-derivative method were employed. A suitable set of trajectories including all possible states at each of the four analyzed E_t was computed for comparing with the quantum calculations. Figure 13 shows the vibrational distribution of the final state of N_2 using TI and QCT methods. The large discrepancies were found at $E_t = 0.804$ eV using the $^3A'$ PES. However, in the QCT calculations at this E_t , only a few trajectories were reactive and the statistics might not be enough. In general, the agreement is quite good.

Table 3 presents the rate coefficient of NO+N computed using the $^3A''$ and $^3A'$ surfaces. The rate coefficients for the formation of N_2 increase with the temperature in the $^3A'$ state faster than in the $^3A''$ case. That is due to the presence of an early barrier in the $^3A'$. At low temperatures this reaction occurs predominantly on the $^3A''$, however, at higher temperatures (e.g. 10000 K), the contribution of both PESs is comparable. The exchange channel is relevant only at high temperatures, due to a barrier at the entry of this channel in both PESs.

In Figure 14, the total rate coefficients for the NO+N \rightarrow N $_2$ +O reaction with others values in the [1000; 5000] K interval reported in the literature are compared. Furthermore, the experimental values recently recommended by the Jet Propulsion Laboratory of Pasadena [62] are included. The Gamallo calculations [45] overestimate the experimental values from 1500 K. The better agreement at lower temperatures could be due to their use of the variational tran-

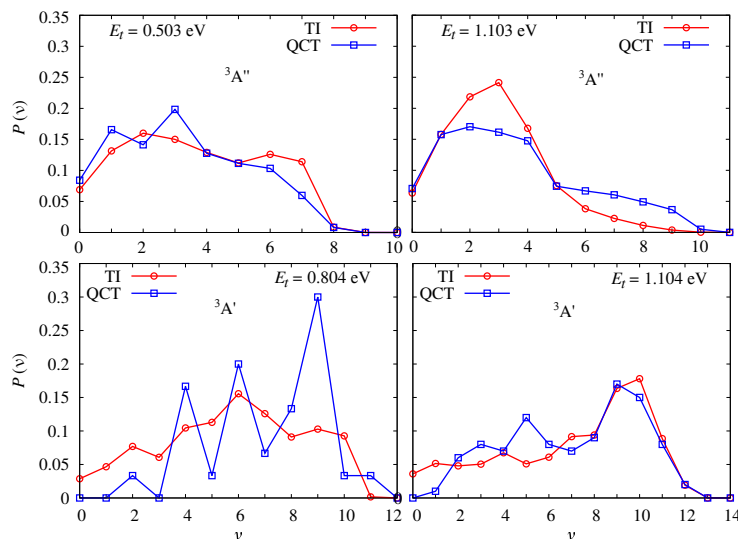


Figure 13: Vibrational distribution $P(\nu)$ of the $\text{NO}+\text{N}\rightarrow\text{N}_2+\text{O}$ reaction using time independent (TI) and QCT methods in both PESs, $^3\text{A}'$ and $^3\text{A}''$.

sition state theory. At low temperatures, the inclusion of the tunnelling and zero points of energies effects are expected to be relevant. The rates coefficients at $T = 100$ K, 200 K, and 300 K were computed, but the discussion in this work will turn on the calculations for $T \geq 1000$ K. Time independent studies are taking place at the moment for analysing the influence of the quantum effects at low temperatures for this reaction. However, at large T the quantum effects should play a smaller role, and the rate coefficients can be determined from QCT calculations.

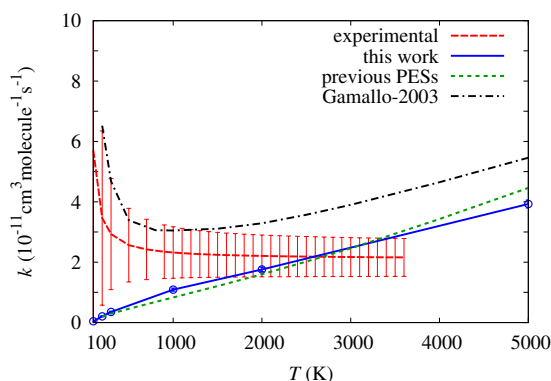


Figure 14: Rate coefficient of the N_2 formation at low temperatures. Experimental data from Ref. [62], the “Gamallo-2003” values were taken from Ref. [45] and “previous PES” was also taken from Ref. [45] but using other surfaces.

The behaviour of the rate coefficients at the temperatures relevant for the hypersonic flight regime is shown in Figure 15. The expected rate increase with increasing T can be seen in Figure 15. Also, the exchange channel become important at high temperatures.

Table 3: Rate coefficients in $\text{cm}^3\text{molecules}^{-1}\text{s}^{-1}$ of the $\text{N}(^4\text{S})+\text{NO}(^2\Pi)$ reaction at several temperatures.

T (K)	$k(^3\text{A}')$	$k(^3\text{A}'')$	$k(^3\text{A}''+^3\text{A}')$
$\text{N}(^4\text{S})+\text{NO}(^2\Pi)\rightarrow\text{N}_2(^1\Sigma)+\text{O}(^3\text{P})$			
1000	9.16×10^{-14}	1.08×10^{-11}	$(1.09 \pm 0.05) \times 10^{-11}$
1000 ^a	2.32×10^{-13}	3.02×10^{-11}	3.05×10^{-11}
1000 ^b	8.10×10^{-15}	8.31×10^{-12}	8.32×10^{-12}
1000 ^c			$(2.32 \pm 0.85)\times 10^{-11}$
2000	1.24×10^{-12}	1.64×10^{-11}	$(1.76 \pm 0.07)\times 10^{-11}$
2000 ^a	2.26×10^{-12}	3.07×10^{-11}	3.29×10^{-11}
2000 ^b	4.17×10^{-17}	1.56×10^{-11}	1.60×10^{-11}
2000 ^c			$(2.24 \pm 0.69)\times 10^{-11}$
5000	9.72×10^{-12}	2.96×10^{-11}	$(3.93 \pm 0.13)\times 10^{-11}$
5000 ^a	7.36×10^{-12}	4.06×10^{-11}	5.46×10^{-11}
5000 ^b	1.41×10^{-11}	3.72×10^{-11}	4.46×10^{-11}
10000	3.13×10^{-11}	4.88×10^{-11}	$(8.01 \pm 0.23)\times 10^{-11}$
15000	4.36×10^{-11}	5.75×10^{-11}	$(1.01 \pm 0.03)\times 10^{-10}$
20000	5.46×10^{-11}	6.81×10^{-11}	$(1.23 \pm 0.03)\times 10^{-10}$
$\text{N}(^4\text{S})+\text{N}'\text{O}(^2\Pi)\rightarrow\text{N}'(^4\text{S})+\text{NO}(^2\Pi)$			
5000	7.22×10^{-13}	1.41×10^{-12}	$(2.13 \pm 0.23)\times 10^{-12}$
5000 ^a	1.19×10^{-12}	5.02×10^{-13}	1.69×10^{-12}
10000	7.04×10^{-12}	1.14×10^{-11}	$(1.85 \pm 0.10)\times 10^{-11}$
15000	1.68×10^{-11}	2.19×10^{-11}	$(3.87 \pm 0.17)\times 10^{-11}$
20000	2.20×10^{-11}	2.75×10^{-11}	$(4.94 \pm 0.21)\times 10^{-11}$

^a Value computed by Gamallo *et al* [45]

^b Value reported in Ref. [45], calculated using previous PESs.

^c Experimental recommended data from Ref. [62]

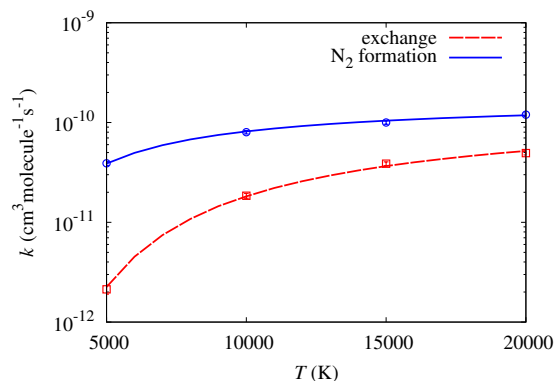


Figure 15: Rate coefficient for the NO+N reaction from 5000 K to 20000 K. The points are the computed rates and the lines corresponded to the expressions 22 and 23.

For modelling re-entry conditions the use of an expression that describes the rate coefficients could be very useful. If the values are fitted to the Arrhenius expression for the exchange rate coefficients, from 5000 to 20000 K it can be

$$k^{exch}(T) = 1.475 \times 10^{-10} \exp(-20907.67/T) \quad (22)$$

In the case of the N₂ formation, this expression from 5000 to 20000 K have the form

$$k(T) = 1.712 \times 10^{-10} \exp(-7423.430/T) \quad (23)$$

Furthermore, a more general expression valid in a largest range of temperatures (1000 K to 20000 K) using the modified Arrhenius expression can be written as

$$k_{mod}(T) = 2.421 \times 10^{-14} T^{0.867} \exp(-102.447/T) \quad (24)$$

3.3 Summary

The two lowest triplet states of N₂O from *ab-initio* calculations at the MRCI+Q level were presented. The energies in each asymptotic channel were fitted using a kernel based method. Furthermore, quasiclassical trajectories calculation using these new PESs were performed up to $T = 20000$ K. The rate coefficients computed in this work were compared with previous studies up to 5000 K. At low temperatures, the quantum effects should play a major role and the rates are not well described from QCT calculations. However, from 1000 K the results of this study are in good agreement with the experimental recommended values. At temperatures lowers than 5000 K the reaction take place mainly in on the ³A'' surface. For higher temperatures, the contribution of both states should be considered. Finally, the Arrhenius expression for the rate coefficient at the extreme temperatures relevant to the hypersonic flight regime for the N₂ formation and the exchange channel are reported.

4 Collision-Induced Rotational Excitation in $\text{N}_2^+(^2\Sigma_g^+, v=0)$ –Ar: Comparison of Computations and Experiment

4.1 Introduction

The collisional dynamics of $\text{N}_2^+(^2\Sigma_g^+)$ cations with Ar atoms is studied using quasi-classical simulations. N_2^+ -Ar is a proxy to study cooling of molecular ions and interesting in its own right for molecule-to-atom charge transfer reactions. An accurate potential energy surface (PES) is constructed from a reproducing kernel Hilbert space (RKHS) interpolation based on high-level *ab initio* data. The global PES including the asymptotics is fully treated within the realm of RKHS. From several ten thousand trajectories, the final state distribution of the rotational quantum number of N_2^+ after collision with Ar is determined. Contrary to the interpretation of previous experiments which indicate that up to 98 % of collisions are elastic and conserve the quantum state, the present simulations find a considerably larger number of inelastic collisions which supports more recent findings.

Cooling neutral and charged atoms and molecules is an essential step for controlled investigations of fundamental processes in chemistry and physics. These methods rely in one way or another on energy transfer between the species to be cooled and their environment. Many techniques to achieve cooling to the millikelvin regime exist. They include, among others, sympathetic cooling of neutral atoms through collisions with laser-cooled species[63] or cooling through collisions with Ar atoms in crossed molecular beams.[64]

An ionic system which is of considerable interest in this context is N_2^+ -Ar. It is a prototypical system to study molecular ions[65, 66] and charge transfer reactions for different internal states of the diatomic.[67] Previous experiments showed that the charge transfer from the molecule to the atom occurs only if N_2^+ is vibrationally excited and no charge transfer is possible for $\text{N}_2^+(v' = 0)$. [65] Figure 16 shows relevant stages for the $\text{N}_2^+(v', j') + \text{Ar} \rightarrow \text{N}_2(v'', j'') + \text{Ar}^+$ reaction.

Another process which takes place on the electronic ground state potential energy surface (PES) is scattering of the Ar atom from the cation through formation of the collision complex $[\text{N}_2\text{Ar}]^+$ (right hand side in Figure 16). Recent experiments of sympathetically cooled N_2^+ ($v = 0, N = 0, J = 0.5$) and collisions with room temperature Ar atoms have shown that the measured rate for quadrupole vibrational excitation of N_2^+ in Coulomb crystals is two orders of magnitude lower than expected.[71] It was speculated that this is due to depopulation of the initially prepared molecular state through rotationally inelastic collisions between the N_2^+ ion and the Ar buffer gas. This process has been previously investigated using laser excited N_2^+ in a 22-pole ion trap in the presence of a low density Ar buffer at 90 K. Specifically, the rotational state $J = 6.5$ of a small number of N_2^+ ions was depopulated via laser induced charge transfer with subsequent observation of refilling the hole via inelastic collisions. Analysis of the experimental data using an advanced kinetic model yields a very low inelastic collision rate ($\leq 2\%$). [65] In order to address these conflicting experimental results and to provide a more atomistically resolved picture, it is desirable to investigate this system using accurate computations. Such an approach has provided further insight into related elementary processes including, e.g., the rotational excitation of N_2^+ through collisions with N_2 , [72] and the reactive collisions of $\text{NO} + \text{O}$ [10, 73] and $\text{OH} + \text{H}$ [74].

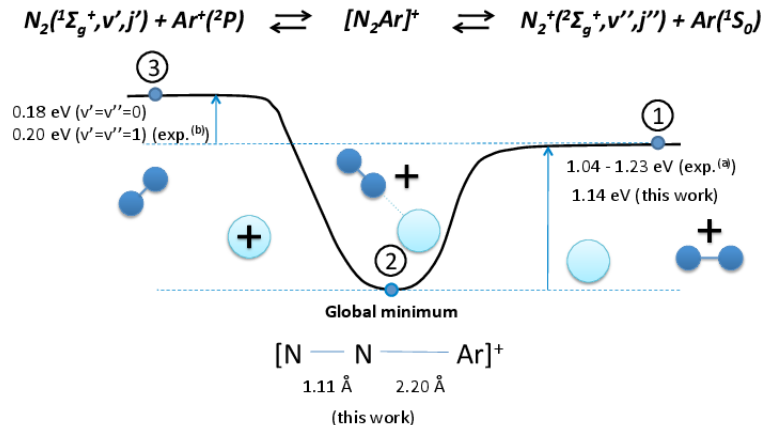


Figure 16: Schematic representation of the relevant stages in the $N_2(v', j') + Ar^+ \rightarrow N_2^+(v'', j'') + Ar$ reaction. Experimentally determined values are indicated by “exp” where the superscript (a) refers to Ref.[68] and (b) to Ref(s).[69, 70] For the vibrational and rotational ground state, the $N_2^+(v'', j'') + Ar$ channel is 0.179 eV below the $N_2(v', j') + Ar^+$ asymptote.[69, 70] The reported experimental dissociation energy of the $[N_2Ar]^+$ complex ranges from 1.04 to 1.23 eV.[68]

The present work focusses on the final state distribution of the rotational quantum number j'' of the N_2^+ ion after collision with Ar starting from a given initial rotational state j' (right hand side in Figure 16). Such simulations provide information about the conservation of the internal state of N_2^+ during and after collisions. Because of the appreciable binding energy of 1.14 eV stabilizing the $[N_2Ar]^+$ complex (see Figure 16), it is expected that the dynamics in the bound state $[N_2Ar]^+$ leads to inelastic collisions and gives rise to rotational excitation. Earlier experimental results suggest the contrary, namely that rotational transitions in $N_2^+ + Ar$ collisions occur rarely and up to 98 % are elastic (“..implies that only one out of 50 collisions results in a change of the rotational state”).[65] A possible explanation for the surprising conservation of the initial rotational state could be the consequence of some hidden constants of motion leading to approximate selection rules.[65]

The collision of N_2^+ molecules with Ar atoms is studied through quasi-classical molecular dynamics (MD) simulations. Hence, quantum effects due to zero-point vibrations and tunneling, which may influence the collisional dynamics and the resulting rotational excitation of N_2^+ , are not included in the simulations. Moreover, rotational fine structure originating from coupling of the spin of N_2^+ and the angular momentum of the diatomic are not included in the present approach. Technically, accurate full close-coupling quantum scattering calculations even for triatomic systems with a deep well (here in excess of 1 eV), large anisotropy of the interaction potential and small rotational constant of the diatomic are currently not feasible. On the other hand, quasi classical trajectory simulations have provided valuable insight into rotational excitation in the related charge exchange reaction $N_2^+ + N_2 \rightarrow N_2 +$

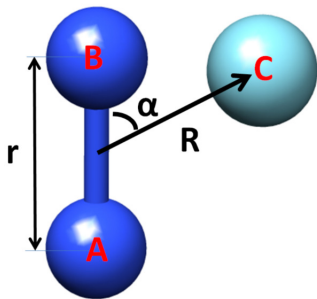


Figure 17: $\text{N}_2^+ + \text{Ar}$ system described in Jacobi coordinates. The dark blue spheres A and B correspond to the nitrogen atoms and the light blue sphere C to the argon atom.

N_2^+ . [72] Similar classical studies have been performed for the $\text{O} + \text{CHD}_3$ system [75] and the hydrogen exchange reaction $\text{OH}^- + \text{HBr} \rightarrow \text{Br}^- + \text{H}_2\text{O}$ without accounting for spin-orbit coupling (as in the present case) and still, good agreement with experiment was obtained. [76] In the light of the computational demands of a fully quantum mechanical treatment and the aforementioned insights obtained for similar systems, a classical treatment appears to be a meaningful approach. To further assess the role of quantum effects, the classical results are complemented with calculations accounting for quantum zero point energy (ZPE) using two different methods.

The ZPE motion of N_2^+ may have non-negligible effects on the results. In particular, since all simulations are carried out within the framework of classical mechanics, ZPE might be consumed and lead to excitation of internal degrees of freedom, which is unphysical. Since there is no unique way to correct for ZPE, [77] two different strategies to probe this are explored: a) trajectories are run on the bare, *ab initio* PES and a binning criterion is applied at the analysis stage, and b) the trajectories are run on a ZPE-corrected PES in order to prevent the unphysical consumption of ZPE during the simulations. Both, a binning criterion [78] and a way to constrain vibrational motion [79, 80] have been previously employed in the literature. The PES is constructed from *ab initio* points using interpolation by the reproducing kernel Hilbert space (RKHS) formalism. [81, 82] Since the present work focuses on the study of rotational transitions in $\text{N}_2^+(v'=0, j') + \text{Ar}$ collisions, only the electronic ground state of N_2^+ is considered.

4.2 Methods

Ab initio calculations

The $\text{N}_2^+ - \text{Ar}$ system is described in Jacobi coordinates, where r is the N-N distance, R is the distance between Ar and the center of mass of the nitrogen atoms, and α is the angle between the direction of R and the N-N axis (see Figure 17).

A total of 3025 points on a regular grid was used to sample the PES at the UCCSD(T) level of theory with an aug-cc-pVTZ basis set [83, 84] using the Gaussian 09 suite of codes. [85] The angular grid corresponds to an 11-point Gauss-Legendre quadrature (α [°] = 11.815, 27.452, 43.089, 58.726, 74.363, 90.000, 105.637, 121.274, 136.911, 152.548, 168.185). [86] For r , the

grid consists of 11 points according to the equilibrium position r_{eq} of the N_2^+ bond and the turning points[87] from $v = 0$ to $v = 4$ ($r = 0.998, 1.010, 1.024, 1.043, 1.071, 1.122, 1.167, 1.207, 1.237, 1.263, 1.287$ Å). The grid of van-der-Waals distances R was chosen to capture the well-region with more densely spaced points and the asymptotic regions with fewer points, for a total of 25 grid points ($R = 1.7, 1.8, 1.9, 2.0, 2.1, 2.2, 2.3, 2.4, 2.5, 2.6, 2.7, 2.8, 2.9, 3.0, 3.1, 3.2, 3.3, 3.4, 3.5, 3.6, 3.8, 4.1, 4.5, 6.0, 9.0$ Å).

The geometry of the $[\text{N}_2\text{Ar}]^+$ complex was optimized and the most stable configuration was found to be linear with Jacobi coordinates of the optimized structure of $r_{\text{eq}} = 1.105$ Å, $R_{\text{eq}} = 2.749$ Å and $\alpha_{\text{eq}} = 0^\circ$. The dissociation energy D_e of the complex in the linear configuration is 1.266 eV with a zero point energy of 0.129 eV (calculated at the UCCSD(T)/aug-cc-pVTZ level of theory). Thus the dissociation energy D_0 of 1.137 eV is in good agreement with the experimentally measured value of 1.109 eV.[88]

RKHS interpolation

In the following only a description of the RKHS formalism is provided for completeness. For more details the reader is referred to the literature.[89]

General procedure

For constructing a multi-dimensional representation of a PES $V(\mathbf{x})$ for a molecular system based on N *ab initio* data points at an arbitrary configuration \mathbf{x} , $V(\mathbf{x})$ is considered to be a bounded function. The quality of the representation of $V(\mathbf{x})$ in terms of a kernel is determined by two aspects: one is the number of grid points which equals the number of kernel coefficients that are used, and the other is the type of kernel function itself. As such, $V(\mathbf{x})$ can be represented in the following fashion

$$V(\mathbf{x}) = \sum_{i=1}^N w_i Q(\mathbf{x}_i, \mathbf{x}) \quad (25)$$

where \mathbf{x}_i are the coordinates of the system at the i -th grid point, w_i are the kernel coefficients, and $Q(\mathbf{x}_i, \mathbf{x})$ is a reproducing kernel.

The multidimensional reproducing kernel $Q(\mathbf{x}, \mathbf{x}')$ can be represented as a product over 1-dimensional kernels.[89] For example, if \mathbf{x} corresponds to the Jacobi coordinates (r, R, α) , the 3-dimensional kernel can be expressed as

$$Q(\mathbf{x}, \mathbf{x}') = q_1(r, r') \cdot q_2(R, R') \cdot q_3(\alpha, \alpha'). \quad (26)$$

where the kernels q_i can be chosen freely depending on the nature of the respective variable (angular or distance-like). The kernel coefficients w_i in Eq. 25 are determined by solving the

following system of linear equations,

$$\begin{bmatrix} Q(\mathbf{x}_1, \mathbf{x}_1) & Q(\mathbf{x}_1, \mathbf{x}_2) & \dots & Q(\mathbf{x}_1, \mathbf{x}_N) \\ Q(\mathbf{x}_2, \mathbf{x}_1) & Q(\mathbf{x}_2, \mathbf{x}_2) & \dots & Q(\mathbf{x}_2, \mathbf{x}_N) \\ \vdots & \vdots & \ddots & \vdots \\ Q(\mathbf{x}_N, \mathbf{x}_1) & Q(\mathbf{x}_N, \mathbf{x}_2) & \dots & Q(\mathbf{x}_N, \mathbf{x}_N) \end{bmatrix} \begin{bmatrix} w_1 \\ w_2 \\ \vdots \\ w_N \end{bmatrix} = \begin{bmatrix} V^{ab \text{ initio}}(\mathbf{x}_1) \\ V^{ab \text{ initio}}(\mathbf{x}_2) \\ \vdots \\ V^{ab \text{ initio}}(\mathbf{x}_N) \end{bmatrix} \quad (27)$$

Since the reproducing kernel matrix is symmetric and positive definite by definition, the computationally efficient Cholesky decomposition can be used to solve Eq. 28.[90] Once the kernel coefficients w_i are known, the energy at an off-grid point \mathbf{x} can be evaluated from Eq. 25.

1-Dimensional Kernels

Distance-like coordinates: In this work, the 1-dimensional kernel for distance-like coordinates was that from Ref.[89],

$$q^{n,m}(x, x') = n^2 x_{>}^{-(m+1)} \times B(m+1, n) {}_2F_1(-n+1, m+1; n+m+1; \frac{x_{<}}{x_{>}}) \quad (28)$$

where $B(m+1, n)$ is the beta function, ${}_2F_1(-n+1, m+1; n+m+1; x_{<}/x_{>})$ is the Gauss hypergeometric function and $x_{<}$ and $x_{>}$ denote the smaller and the larger of x and x' respectively. The chosen value for n controls up to which derivative the kernel is smooth, while the value of m controls its long-range behaviour.[89] In particular, if no points are available in the asymptotic region, m can be chosen to mimic the physical long-range behaviour of the interpolated variable. Here we use $n = 2$ and $m = 6$ for both distance-like kernels, although different values are possible.[91] In the present work the choice of m is largely inconsequential because enough data is available in asymptotic regions and the *ab initio* points are necessarily reproduced exactly.

Angle-like coordinates: For angle-like internal coordinates the general expression for the kernel is[89]

$$q^n(x, x') = \sum_{i=0}^{n-1} x_{>}^i x_{<}^i + n x_{<}^n x_{>}^{n-1} {}_2F_1(1, -n+1; n+1; \frac{x_{<}}{x_{>}}) \quad (29)$$

Eq. 29 is valid only if the angle-like coordinate is rescaled so that both x and x' belong to the interval $[0, 1]$. For example, to rescale the Jacobi coordinate α a new coordinate y is defined as $y = (1 - \cos \alpha)/2$. Again, choosing $n = 2$ is sufficient for an accurate representation of the angular dependence.

Treatment of the Asymptotics

The 1-dimensional distance-like kernel given by Eq. 29 has the advantage that it correctly decays to zero at long range. While this is still true in the present case for one particular value of the N-N separation r , this is not the case for the total energy of the complex for arbitrary

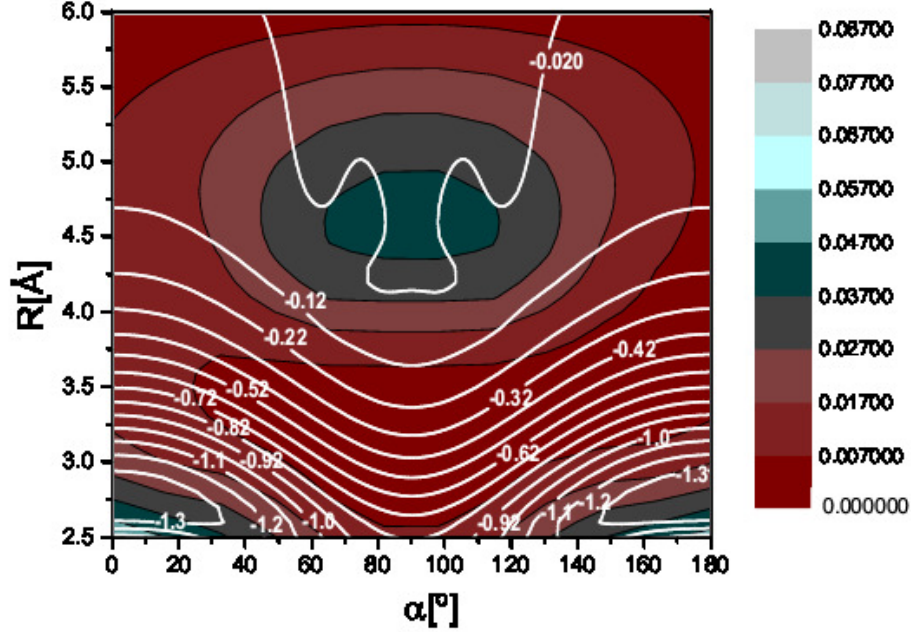


Figure 18: Contour plot of the RKHS interpolated N_2^+ -Ar PES (white lines) with N_2^+ at its equilibrium position ($r_{eq} = 1.122$ Å). The binding energy is around 1.3 eV and isocontours are labelled with energies in eV. The color map is the error surface with relative errors in %. Relative errors were obtained by comparing the interpolated energies to off-grid *ab initio* data. Even the largest relative errors are below 0.1 %.

values of r . The correction of the asymptotics was considered in previous work on HO_2 by using a manybody expansion of the PES.[92] For the present work, a different method, which is fully within the RKHS formalism, was used and is presented in Section 4.3.

Correction of ZPE in the N_2^+ -Ar PES One way to account for ZPE in the simulations is to carry out a point-wise correction of the PES whereby the ZPE contribution is taken into account at each configuration.[93] This contribution is calculated from the harmonic oscillator energy evaluated for $n = 0$

$$V^{ZPE} = \sum_{i=1}^N \left(\frac{1}{2} + n \right) \hbar \omega_i \quad (30)$$

where $N = 3$ is the number of degrees of freedom of the system and ω_i are the positive eigenvalues obtained from *ab initio* calculations at the MP2/aug-cc-pVTZ level of theory.

In the present simulations two different PESs were employed, one where the ZPE correction given by Eq. 30 is included (*ZPE-corrected PES*) and one where no such correction was made (*bare PES*). The RKHS PES and its quality compared to off-grid points is shown in Figure 18.

Molecular Dynamics Simulations

MD simulations of the collision between N_2^+ and Ar have been carried out with CHARMM.[94] The equations of motion were integrated using a time step of $\Delta t = 0.1$ fs and energies were calculated from the RKHS representation of the PES described in Section 4.2 using the bare and ZPE-corrected PESs, respectively. Forces were obtained by numerical differentiation using a five-point stencil.[95]

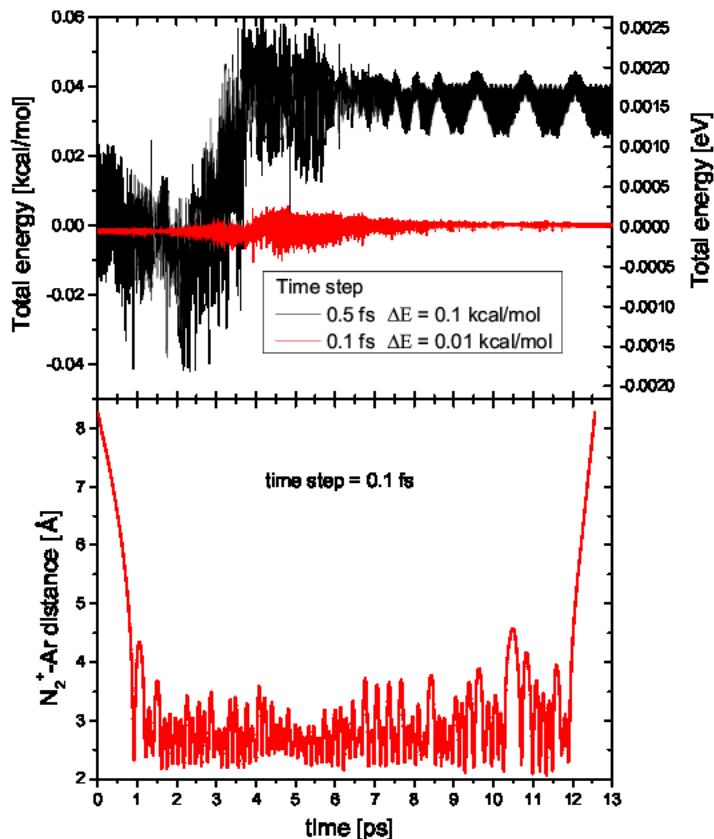


Figure 19: A representative molecular dynamics simulation for the collision between N_2^+ and Ar. The upper panel reports the variation of the total energy as a function of time for time steps $\Delta t = 0.5$ and 0.1 fs, respectively. In the bottom panel the distance between the ion and the incoming Ar atom is shown for $\Delta t = 0.1$ fs. After ≈ 0.5 ps the complex is formed and lives for about 12.5 ps after which it breaks up again.

Initial conditions were generated from a WKB-quantized periodic orbit of the corresponding rotating Morse oscillator for given vibrational v and rotational j quantum numbers.[16, 96] Parameters for the Morse potential were fitted to *ab initio* data for N_2^+ ($D_e = 8.5003$ eV, $r_e = 1.1307$ Å, $\beta = 2.5928$ Å $^{-1}$). The fitted dissociation energy is consistent with the experimental value of 8.724 eV.[97] The initial vibrational quantum number was $v' = 0$ and the rotational quantum numbers were either $j' = 0$ or $j' = 6$. Relative collision energies between

N_2^+ and Ar were sampled from a Maxwell-Boltzmann distribution at either 90 K or 300 K. These initial conditions are representative of the previous experiments which investigate $[\text{N}_2^+ (v' = 0, j' = 6); T = 90 \text{ K}]$ [65] and the collision of ultracold molecular ions with Ar at room temperature $[\text{N}_2^+ (v' = 0, j' = 0); T = 300 \text{ K}]$. [71] The impact parameter b was selected from a uniform distribution between 0 and $25 a_0$ (prior test runs had shown that larger impact parameters do not lead to collision or even mutual influence of the impact partners). Such a procedure was already employed in previous studies of the collisions between $\text{O}(^3\text{P})$ and $\text{NO}(^2\Pi)$. [10]

Simulations on the ZPE-corrected PES used a suitably modified procedure for generating initial conditions for the positions and velocities. For $v' = 0$ and any j' , the position is always set to the minimum of the effective Morse potential $V_{\text{eff}}(r) = V(r) - \frac{j'(j'+1)}{r^2}$ and all vibrational energy is removed from the N-N stretch as the ZPE is already accounted for in the corrected PES. The vibrational energy corresponding to the ZPE is added back prior to the analysis in order to be able to use the same filtering criteria for the ZPE-corrected and bare PES.

All trajectories were run until the collision partners were fully separated, for which a value corresponding to more than 1.3-times their initial separation was assumed. The maximum simulation time considered was 1 ns. For statistically significant results a total of 25000 trajectories was run for each temperature and PES and approximately 4000 of them were excluded from the analysis due to lifetimes longer than 1 ns.

4.3 Results

Correction of the asymptote

Depending on the N_2^+ bond length r individual manifolds $V(R, \alpha; r)$ dissociate to different asymptotic values for $R \rightarrow \infty$. This assumes that the PES becomes isotropic (α -independent) with increasing R which is in general true. In order to employ RKHS interpolation in a meaningful fashion for the R - and α - degrees of freedom, the asymptotic value for each manifold characterized by a specific value for the N-N separation must be shifted to zero energy. This is necessary because kernels decay to zero asymptotically.

In order to set the energy to zero for every cut ($r = \text{constant}$), the energy of the isolated diatomic $E(r, R \rightarrow \infty)$ is subtracted from the energy of all points that share the same value of r and yields $V^{\text{new}}(r, R, \alpha) = E(r, R, \alpha) - E(r, R \rightarrow \infty)$ and $V^\infty(r) = E(r, R \rightarrow \infty)$. The two data sets $V^{\text{new}}(r, R, \alpha)$ and $V^\infty(r)$ are then interpolated within the RKHS framework. Because the PES is isotropic for sufficiently large R , the interpolation of $V^\infty(r)$ requires only a 1-dimensional kernel. Hence, all quantities required are represented by kernels and the global PES can be evaluated at an off-grid point (r^0, R^0, α^0) according to Eq. 31.

$$V(r^0, R^0, \alpha^0) = V^{\text{new}}(r^0, R^0, \alpha^0) + V^\infty(r^0) \quad (31)$$

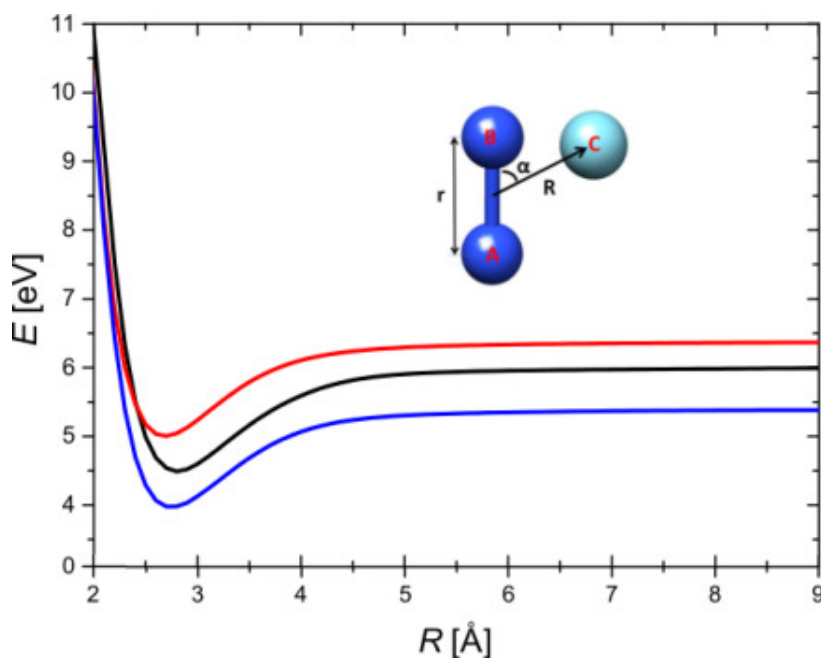


Figure 20: Part of the global PES for a triatomic system $\text{N}_2^+\text{-Ar}$. The relevant coordinates (r, R, α) are indicated in the inset with the dark blue spheres corresponding to the N_2^+ molecule and the light blue sphere to the Ar atom. The three curves refer to different intermolecular distances of the diatomic N_2^+ (r_{NN}), $r_{\text{NN}} = 1.00 \text{ \AA}$ (red), $r_{\text{NN}} = 1.11 \text{ \AA}$ (blue) and $r_{\text{NN}} = 1.21 \text{ \AA}$ (black). In the quantum chemistry calculations the asymptotes of each manifold characterized by the particular r_{NN} separation dissociates to its own asymptote as indicated by the non-overlapping curves at long range. If the asymptote is not corrected in the RKHS interpolation, all curves converge to a value of $E = 0$ for large R .

Simulation and Analysis of Collisional Excitation

Simulations on the bare and ZPE-corrected PES were carried out with a range of initial conditions. The physical conditions included two temperatures, $T = 90$ K and $T = 300$ K. The first corresponds to previous experiments[65] and the latter was chosen to examine the role of temperature on the results. The time step in all simulations was $\Delta t = 0.1$ fs. Overall, 25000 trajectories were run for each temperature. However, a considerable number of trajectories are not further analyzed because they violate in one way or another restrictions imposed by quantum mechanics. Such filtering at the post-processing stage is a usual procedure to limit the number of classical trajectories to be analyzed to those which correspond to valid simulations within a semiclassical framework.

Filtering at the post-processing stage was carried out as follows. The WKB procedure can be used to determine the vibrational quantum number v'' on the effective potential. In general a real, non-integer number is obtained for v'' . By applying a binning criterion, only trajectories with v'' within certain thresholds are retained for further analysis. This ensures that only trajectories are analyzed in which ZPE was not transformed to other forms of energy during the simulation. Three different thresholds were used here: $\text{frac}(v'') = \pm 0.1, \pm 0.01$ and ± 0.001 , where $\text{frac}(x)$ is the difference of x to the closest integer value. These values correspond to a conservation of the ZPE within 220.70 cm^{-1} , 22.07 cm^{-1} and 2.21 cm^{-1} , respectively.

Rotational j'' states are rounded to the next closest integer value divisible by 2 in order to fulfill restrictions imposed by the symmetry of N_2^+ , which can exist in either the *ortho* or *para* nuclear spin state. If a binning criterion similar to the vibrational quantum number is applied to j'' states, the number of trajectories that fulfill both criteria decreases dramatically. Hence, no such binning was applied for j'' . For the final state analysis of trajectories run on the corrected PES, the ZPE is added back into the classical rovibrational energy, since it was removed before generating the initial conditions.

The final distribution of j'' states, $P(j'')$, is determined from the WKB procedure after the complex has dissociated. An event is classified as “inelastic” if the final j'' differs from the initial j' , i.e. $j'' \neq j'$. As the simulations involve numerical imprecisions of about 3.5 cm^{-1} (see Figure 19, upper panel), corresponding to roughly the energy difference between $j' = 0$ to $j'' = 1$ for N_2^+ (based on a rotational constant of $B = 1.932 \text{ cm}^{-1}$)[98], an additional criterion on the necessary amount of change in j'' was introduced to classify inelastic transitions. For this, the quantity j^* is used. Only trajectories for which the final j'' differs by more than j^* from the initial j' state are considered to correspond to an inelastic collision.

Rotational excitation Figure 21 reports the final state distribution $P(j'')$ for N_2^+ from simulations on the bare and ZPE-corrected PES starting from $j' = 0$. Results are presented for simulations at $T = 90$ K and $T = 300$ K. The distributions differ slightly between the two PESs while temperature has only a minor effect on $P(j'')$. On the bare PES higher j'' -states are populated compared to simulations on the ZPE-corrected PES. Possibly, this is due to the more isotropic shape of the ZPE-corrected PES due to angular averaging. Also, as the well is more shallow on the ZPE-corrected PES due to inclusion of ZPE, the anisotropy near the inner wall is less accessible. The maximum of the distribution is at $j'' = 2$, whereas it is at $j'' = 0$ for the bare PES. This already suggests that more than a fraction (i.e. 2% in the

experiments[65]) of the collisions are inelastic.

The distribution changes only slightly between different filtering criteria, as is shown in the inset in Figure 21. The percentage of inelastic and elastic collisions for the bare PES and a filtering criterion of $\text{frac}(v'') = \pm 0.01$ is summarized in Table 4. A collision is inelastic if the rotational quantum number of the diatomic differs from the initial j' by more than j^* , i.e. $j'' \notin [j' - j^*, j' + j^*]$. Even with an unrealistically large margin of $j^* = 4$, the fraction of inelastic collisions is well above the experimentally reported value of 2 %.[65] Depending on the figure of merit j^* used, 20 % to 40 % of collisions are inelastic, see Table 4.

Figure 22 shows the correlation between impact parameter b and j'' states. It is typically found that smaller impact parameters lead to higher rotational excitation whereas collisions with large b are preferentially elastic.

A remarkable result is that excitation to the highest rotational states is only found for trajectories with shorter lifetimes (see Figure 23). Closer examination of some individual trajectories with short lifetime shows that no tight $[\text{N}_2\text{Ar}]^+$ complex has to be formed for rotational excitation of N_2^+ to occur. A “tight complex” refers to a situation in which the collision partners come close enough to at least once enter the short-range repulsive region of the interaction potential. For rotational excitation it is sufficient for the two collision partners to fly past each other such as to influence their respective flight paths. The interaction between N_2^+ and Ar leads to a torque which results in pronounced rotational excitation of N_2^+ . Such “fly-by” trajectories (lifetime of the complex shorter than 5 ps) lead to excitation to higher rotational states than trajectories with a longer lifetime and make up 21.5 % of all trajectories.

Counter-intuitively, the impact parameter b is not correlated to the lifetime of the complex (see inset of Figure 22). In fact, the complex can be formed and live for a very long time even for large impact parameters, provided that the collision energy is sufficiently low. Conversely, small impact parameters still sometimes lead to fly-by trajectories, provided that the collision energy is sufficiently large. It is the combination of a small impact parameter and a high collision energy (leading to fly-by trajectories) that leads to the highest rotational excitations.

	elastic (%)	inelastic (%)
bare PES		
$T = 90 \text{ K } (j^*=2)$	63	37
$T = 300 \text{ K } (j^*=2)$	67	33
$T = 90 \text{ K } (j^*=4)$	70	30
$T = 300 \text{ K } (j^*=4)$	79	21
ZPE-corrected PES		
$T = 90 \text{ K } (j^*=2)$	64	36
$T = 300 \text{ K } (j^*=2)$	60	40
$T = 90 \text{ K } (j^*=4)$	86	14
$T = 300 \text{ K } (j^*=4)$	78	22

Table 4: Percentage of elastic and inelastic collisions for a filtering criterion of $\text{frac}(v') = 0.01$ with initial $j = 0$. A collision is considered as inelastic when j' changes from 0 to $j'' > j^*$.

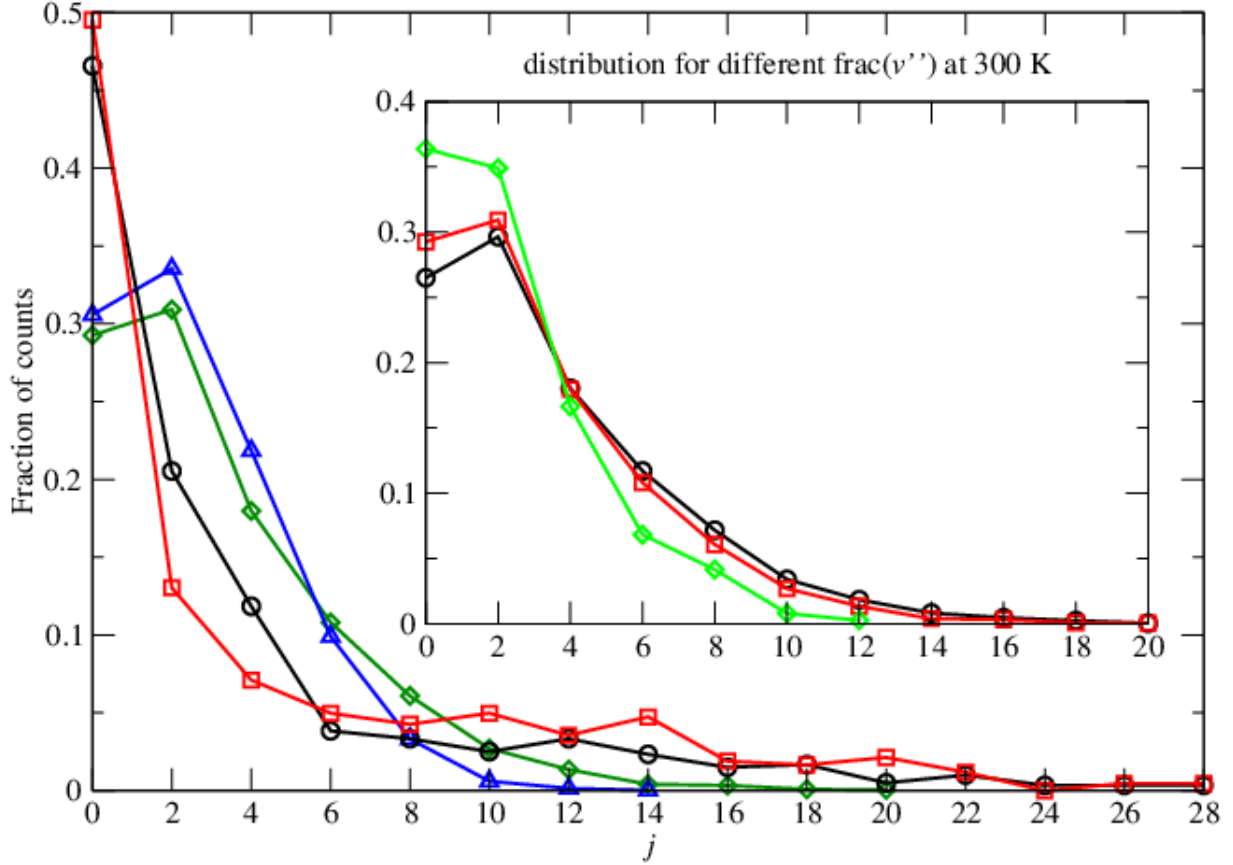


Figure 21: *Green diamonds (ZPE-corrected, 300 K), blue triangles (ZPE-corrected, 90 K), black circles (bare, 300 K), red squares (bare, 90 K).* Distribution of j'' states after dissociation for ZPE conservation criterion $\text{frac}(v'') = \pm 0.01$ and different temperatures. Trajectories were started with an initial $j' = 0$ and evolved on the bare and ZPE-corrected PES. The total count of trajectories that meet the conservation criterion are 4207 ($T = 300$ K) and 3309 ($T = 90$ K) on the corrected and 599 ($T = 300$ K) and 422 ($T = 90$ K) on the bare PES, respectively. Note that trajectories on the corrected PES are much more likely to meet the criterion, because ZPE is removed during the dynamics and added back in the analysis. As such, the conservation criterion on the corrected PES can only be violated by an uptake of energy, whereas it can be violated by an uptake or loss of energy on the bare PES. *Inset:* Distribution of j'' states after dissociation for different ZPE conservation criteria ($\text{frac}(v'') = \pm 0.1$, black circles, $\text{frac}(v'') = \pm 0.01$, red diamonds, $\text{frac}(v'') = \pm 0.001$, green squares) at $T = 300$ K on the ZPE-corrected PES. The number of trajectories that meet the criterion are 19821, 4207 and 745, respectively. The distribution changes slightly, but shows the same overall behaviour for the different filtering criteria.

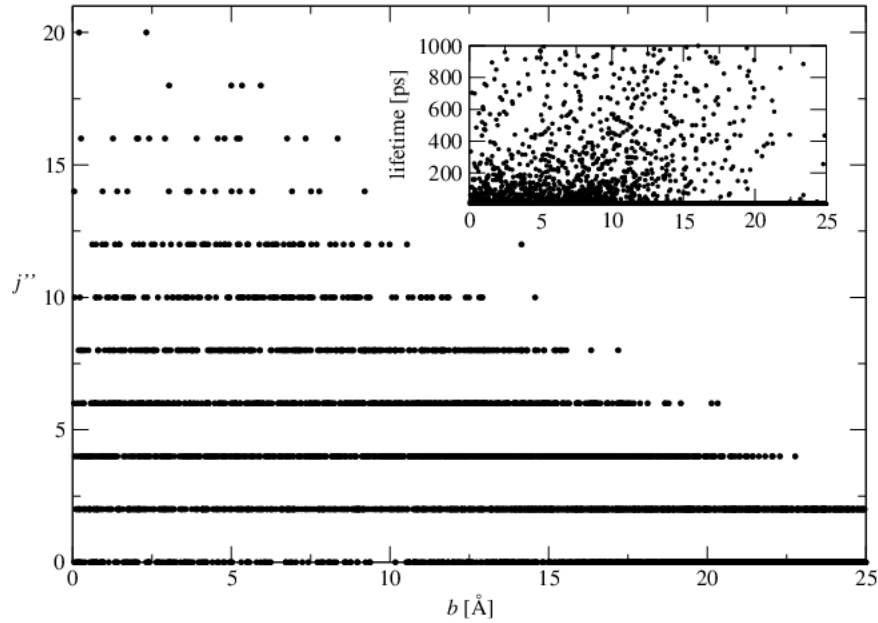


Figure 22: Impact parameter b *vs.* j'' ($j' = 0$, $T = 300$ K) on the corrected PES. Large rotational excitation is observed only for small impact parameters. Plots for other temperatures on the corrected and bare PES show similar behaviour. Impact parameter b *vs.* lifetime. The lifetime is not correlated to the impact parameter (inset).

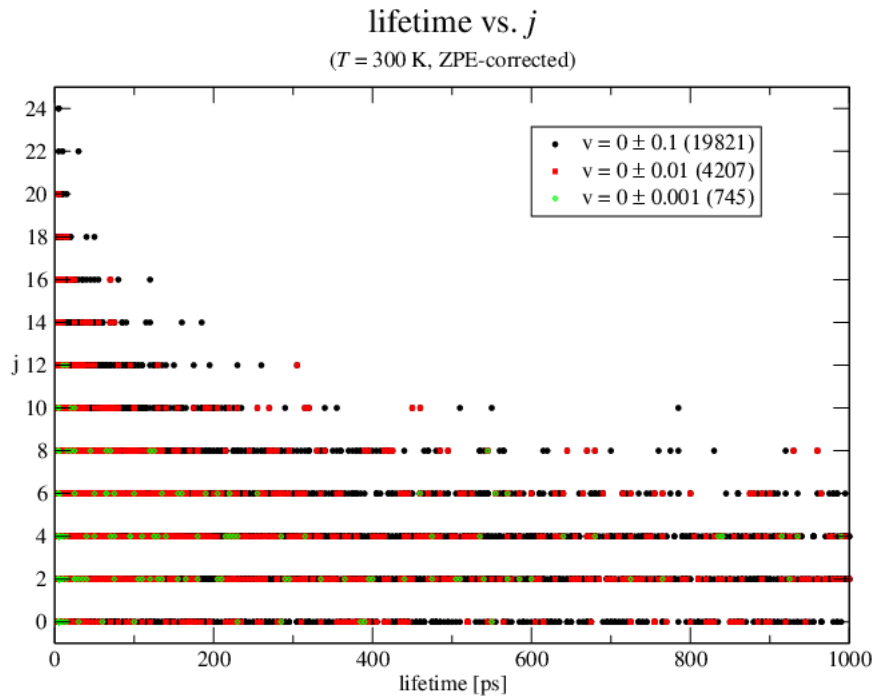


Figure 23: Lifetime *vs.* j'' ($j' = 0$, $T = 300$ K) on the corrected PES for different ZPE conservation criteria, numbers in parentheses indicate how many trajectories meet the criterion. The largest rotational excitation is observed only for short lifetimes. Plots for other temperatures on the corrected and bare PES show similar behaviour.

The earlier experiments[65] were thermal and started from a distribution of rotational states, but the initial rotational state studied was $j' = 6$. Hence, additional simulations were carried out for this case. 25000 independent trajectories were started on the ZPE-corrected PES. Figure 24 shows the distribution of j'' states after the complex dissociates. The percentage of inelastic collisions for the strictest filtering criterion $\text{frac}(v'') = \pm 0.001$ and $j^* = 0$ is 41 % and decreases to 17 % for $j^* = 2$, respectively. The rate constant for rotational excitation/relaxation was calculated according to[10]

$$k(T) = \sqrt{\frac{8}{\pi\mu\beta}} \frac{2\pi b_{\max}}{g(T)N_{\text{tot}}} \sum_{i=1}^{N_{\text{reac}}} b_i \quad (32)$$

where μ is the reduced mass of the $\text{N}_2^+ - \text{Ar}$ complex, $g(T)$ is the electronic degeneracy factor, b_{\max} is the maximum impact parameter, b_i the impact parameter of trajectory i , N_{tot} the total number of trajectories that meet the filtering criterion, N_{reac} the number of inelastic trajectories ($|j'' - j'| > j^*$) and $\beta = 1/(k_B T)$. The calculated value of $k_{j'=6 \rightarrow j'' \neq 6} = 1.17 \cdot 10^{-9} \text{ cm}^3 \text{ s}^{-1}$ is two orders of magnitude larger than the reported value of $k = (1.4 \pm 0.4) \cdot 10^{-11} \text{ cm}^3 \text{ s}^{-1}$. [65] However, it should be noted that the experimental value was not directly measured, but inferred from a kinetic model based on the rate coefficient for charge transfer and the rate of laser excitation.

Since the Langevin rate is often considered to be an upper bound for reaction rates it is surprising that the *computationally determined* rate $k_{j'=6 \rightarrow j'' \neq 6}$ is about 60 % larger than the Langevin rate $k_L = 7.4 \cdot 10^{-10} \text{ cm}^3 \text{ s}^{-1}$. [65] However, rates larger than k_L have been reported previously in the literature[99]. It should be noted that Langevin theory assumes an idealized form for the centrifugally corrected interaction potential between the ion, which is modelled as a point charge, and the neutral atom given by[100]

$$V_L(R) = \frac{1}{2} \frac{L^2}{\mu R^2} - \frac{\alpha' e^2}{8\pi\epsilon_0 R^4} \quad (33)$$

where $L = \mu v b$, v is the relative collision velocity, α' the polarizability volume of the neutral species, μ the reduced mass, b the impact parameter and R the distance between centre of mass of the molecular ion and neutral species. A comparison between the $1/R^4$ term in Eq. 33 and the actual interaction potential shows that Langevin theory is insufficient to describe the collisional rate. In particular, the true PES decays more slowly to zero and the anisotropy of the PES (see Figure 18), which is crucial for the dynamics, is completely neglected in the Langevin model. Nonetheless, if Langevin theory is applied naively to the same set of trajectories that was used to calculate the $k_{j'=6 \rightarrow j'' \neq 6}$ rate and Eq. 32 is used to calculate a rate (counting those trajectories as "reactive" that satisfy $E_C \geq V_L(R_{\max})$, where E_C is the collision energy and $V_L(R_{\max})$ is the Langevin interaction potential at the position of the maximum of the centrifugal barrier according to Langevin theory), a rate constant of $k_L = 6.2 \cdot 10^{-10} \text{ cm}^3 \text{ s}^{-1}$ is obtained. This is in good agreement with the value of $k_L = 7.4 \cdot 10^{-10} \text{ cm}^3 \text{ s}^{-1}$ from Langevin theory. Note however that this analysis can be performed from the initial conditions without running actual dynamics and merely shows that the initial conditions for our simulations are consistent with the Langevin model. However, the model itself is insufficient to describe the actual dynamics. It should also be considered that k_L measures merely a sort of "collision rate", but as was pointed out earlier, the complex

does not need to be formed in order for rotational relaxation or excitation to occur. In fact, for 92.4 % of the trajectories the Langevin model correctly predicts whether the complex is formed or not from just the initial conditions. Since the observed rate is 60 % larger than the Langevin rate, this further indicates that rotational excitation can occur without complex formation. A final test was to run simulations with an explicitly isotropic PES beyond 8 Å. At this distance, the PES is still appreciably anisotropic ($\approx 50 \text{ cm}^{-1}$ between linear and T-shape geometry). Hence, the PES was multiplied by an empirical factor of $\exp(-(R/7.3\text{Å})^{20})$, which ensures a smooth cutoff at long-range, yet leaving the short-range part of the PES largely unaffected. Although this PES fulfills the requirement of Langevin theory, namely that the long range part of the PES should be isotropic, the computed rate is unaffected and still exceeds the Langevin rate. It is suspected that the anisotropy in the range below 8 Å is the main cause for rotational excitation.

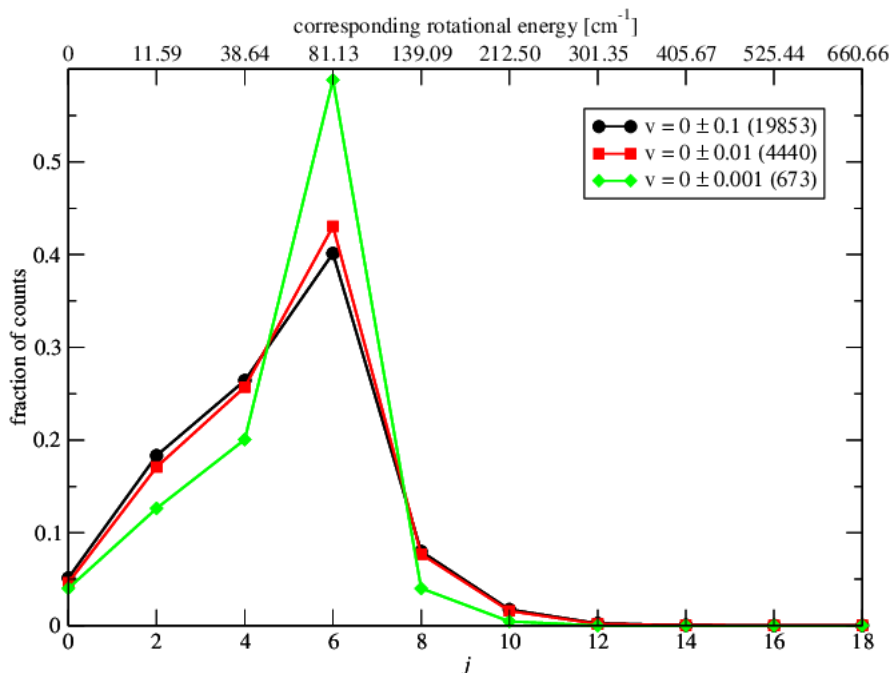


Figure 24: Distribution of j'' states after dissociation for different ZPE conservation criteria at $T = 90 \text{ K}$. The numbers in brackets show how many trajectories meet the criterion. For every value of j , the corresponding rotational energy is given (the rotational constant is $B = 1.932 \text{ cm}^{-1}$).[98] Trajectories were started with an initial $j' = 6$ and evolved on the ZPE-corrected PES.

4.4 Conclusion

Classical molecular dynamics simulations of the nonreactive collision between the N_2^+ cation and Ar atoms at two different temperatures show that inelastic rotational excitation of the ion in the product channel is important and occurs more frequently than previously assumed. The simulations use an RKHS PES based on UCCSD(T)/aug-cc-pVTZ electronic structure calculations and correct handling of the asymptotics within the RKHS framework. Analysis of

the results for $j' = 6$ using a strict filtering criterion of $\text{frac}(v'') = \pm 0.001$ and a figure-of-merit $j^* = 2$ suggests that inelastic collisions occur in at least 17 % of the cases which is one order of magnitude larger than reported in earlier experiments (2 %).^[65] Interestingly, the $[\text{N}_2\text{Ar}]^+$ complex does not need to be formed (and stabilized) for rotational excitation to occur. A sufficiently close encounter of the two collision partners is sufficient to mutually influence their flight paths and lead to rotational excitation. It should be pointed out that the PES used in this work was calculated using a single-reference method. Electronic effects, which are not adequately captured using single-reference methods, might play a non-negligible role in the dissociative region of the PES. Consequently, further investigations should employ multi-reference methods such as MRCI to capture electronic effects which are, however, outside the scope of the present work. For a complete understanding of the rate of rotational excitation in the N_2^+-Ar system, new experiments, which allow precise control of the exact quantum state of the collision partners and additional computational investigations at the quantum level are necessary.^[71]

Acknowledgments

Part of this work was supported by the United State Department of the Air Force which is gratefully acknowledged (to JCCP). Support by the Swiss National Science Foundation through grants 200021-117810, the NCCR MUST (to MM), and the University of Basel is also acknowledged.

References

- [1] Castro-Palacio, J. C.; Bemish, R. J.; Meuwly, M. *J. Chem. Phys.* **2015**, *142*(9), 091104.
- [2] Unke, O. T.; Castro-Palacio, J. C.; Bemish, R. J.; Meuwly, M. *J. Chem. Phys.* **2016**, *144*(22), 224307.
- [3] Denis-Alpizar, O.; Bemish, R. J.; Meuwly, M. **2016**, *in preparation*.
- [4] Yoshino, K.; Esmond, J.; Parkinson, W. *Chem. Phys.* **1997**, *221*(1,2), 169–174.
- [5] Schneider, W.; Moortgat, G.; Tyndall, G.; Burrows, J. *J. Photochem. Photobiol. A* **1987**, *40*(2,3), 195–217.
- [6] Corcoran, T.; Beiting, E.; Mitchell, M. *J. Molec. Spectrosc.* **1992**, *154*(1), 119–128.
- [7] Schwartzentruber, T.; Scalabrin, L.; Boyd, I. *J. Spacecraft Rockets* **2008**, *45*(6), 1196–1206.
- [8] Gordon, S.; McBride, B. J. *NASA Reference Publication* **1996**, page 1311.
- [9] McBride, B.; Zehe, M.; Gordon, S. *NASA report TP-2002-211556* **2002**.
- [10] Castro-Palacio, J.; Nagy, T.; Bemish, R.; Meuwly, M. *J. Chem. Phys.* **2014**, *141*, 164319.
- [11] Harding, L.; Stark, H.; Troe, J.; Ushakov, V. *Phys Chem Chem Phys.* **1999**, *1*(1), 63–72.

- [12] Atkins, P.; de Paula, J. *Atkins' Physical Chemistry, 8th edition*; W.H. Freeman, New York, 2006.
- [13] Ho, T. S.; Rabitz, H. *J. Chem. Phys.* **1996**, *104*(7), 2584–2597.
- [14] Levine, R. D. *Molecular Reaction Dynamics*; Cambridge University Press, Cambridge, 2005.
- [15] Duff, J.; Sharma, R. D. *J. Chem. Soc., Faraday Trans.* **1997**, *93*, 2645–2649.
- [16] Porter, R. N.; Raff, L. M.; Miller, W. H. *J. Chem. Phys.* **1975**, *63*(5), 2214–2218.
- [17] Frenkel, D.; Smit, B. *Understanding Molecular Simulation. From Algorithms to Applications (2nd Edition)*; Academic Press, London, 2001.
- [18] McNaught, A. D.; Wilkinson, A. *IUPAC. Compendium of Chemical Terminology, 2nd ed. (the Gold Book)*; Blackwell Scientific Publications, Oxford, 1997.
- [19] Valli, G.; Orru, R.; Clementi, E.; Lagana, A.; Crocchianti, S. *J. Chem. Phys.* **1995**, *102*, 2825–2832.
- [20] Baulch, D.; Cobos, C.; Cox, R.; Frank, P.; Hayman, G.; Just, T.; Kerr, J.; Murrells, T.; Pilling, M.; Troe, J.; Walker, R.; Warnatz, J. *J. Phys. Chem. Ref. Data* **1994**, *23*, 847–1033.
- [21] Bose, D.; Candler, G. V. *J. Chem. Phys.* **1997**, *107*(16), 6136–6145.
- [22] Huang, J.; Buchowiecki, M.; Nagy, T.; Vanicek, J.; Meuwly, M. *Phys Chem Chem Phys.* **2014**, *16*, 204–211.
- [23] Clark, T.; Garnett, S. H.; Kistiak, G. B. *J. Chem. Phys.* **1969**, *51*, 2885–2891.
- [24] Gurvich, L.; Veyts, I.; Alcock, C. *Thermodynamic Properties Of Individual Substances, 4th ed.*; Hemisphere Publishing Corp., Washington, DC, 1989.
- [25] Armenise, I.; Esposito, F. *Chem. Phys.* **2015**, *446*, 30–46.
- [26] Li, J.; Varandas, A. J. *J. Phys. Chem. A* **2012**, *116*(18), 4646–4656.
- [27] Li, J.; Caridade, P. J.; Varandas, A. J. *J. Phys. Chem. A* **2014**, *118*(8), 1277–1286.
- [28] González, M.; Valero, R.; Sayós, R. *J. Chem. Phys.* **2000**, *113*(24), 10983–10998.
- [29] Black, G.; Slinger, T.; St John, G.; Young, R. *J. Chem. Phys.* **1969**, *51*, 116–121.
- [30] Lin, C.-L.; Kaufman, F. *J. Chem. Phys.* **1971**, *55*(8), 3760–3770.
- [31] Fell, C.; Steinfeld, J.; Miller, S. *J. Chem. Phys.* **1990**, *92*(8), 4768–4777.
- [32] Husain, D.; Kirsch, L.; Wiesenfeld, J. **1972**, *53*, 201–210.
- [33] Husain, D.; Mitra, S. K.; Young, A. N. *J. Chem. Soc., Faraday Trans. 2* **1974**, *70*, 1721–1731.

- [34] Sugawara, K.-i.; Ishikawa, Y.-i.; Sato, S. *Bull. Chem. Soc. Jpn.* **1980**, *53*(11), 3159–3164.
- [35] Wennberg, P. O.; Anderson, J. G.; Weisenstein, D. K. *J. Geophys. Res. Atmos.* **1994**, *99*(D9), 18839–18846.
- [36] Jeoung, S. C.; Choo, K. Y.; Benson, S. W. *J. Phys. Chem.* **1991**, *95*(19), 7282–7290.
- [37] Lee, J.; Michael, J.; Payne, W.; Stief, L. *J. Chem. Phys.* **1978**, *69*(7), 3069–3076.
- [38] Clyne, M. A.; McDermid, I. S. *J. Chem. Soc., Faraday Trans. 1* **1975**, *71*, 2189–2202.
- [39] Kistiakowsky, G.; Volpi, G. *J. Chem. Phys.* **1958**, *28*(4), 665–668.
- [40] FOX, J. *J. Geophys. Res. Phys.* **1994**, *99*(A4), 6273–6276.
- [41] Bergeat, A.; Hickson, K. M.; Daugey, N.; Caubet, P.; Costes, M. *Phys Chem Chem Phys.* **2009**, *11*(37), 8149–8155.
- [42] Hopper, D. G. *J. Chem. Phys.* **1984**, *80*(9), 4290–4316.
- [43] Bose, D.; Candler, G. V. *J. Chem. Phys.* **1996**, *104*(8), 2825–2833.
- [44] Bose, D.; Candler, G. V. *J. Thermophys Heat Transfer* **1996**, *10*(1), 148–154.
- [45] Gamallo, P.; González, M.; Sayós, R. *J. Chem. Phys.* **2003**, *119*(5), 2545–2556.
- [46] Gamallo, P.; Sayós, R.; González, M.; Petrongolo, C.; Defazio, P. *J. Chem. Phys.* **2006**, *124*(17), 174303.
- [47] Lin, W.; Varga, Z.; Song, G.; Paukku, Y.; Truhlar, D. G. *J. Chem. Phys.* **2016**, *144*(2), 024309.
- [48] Lin, W.; Meana-Pañeda, R.; Varga, Z.; Truhlar, D. G. *J. Chem. Phys.* **2016**, *144*(23), 234314.
- [49] Langhoff, S. R.; Davidson, E. R. *Int. J. Quantum Chem.* **1974**, *8*(1), 61–72.
- [50] Dunning, T. H. *J. Chem. Phys.* **1989**, *90*, 1007.
- [51] Werner, H. J.; Knowles, P. J.; Knizia, G.; Manby, F. R.; Schütz, M. *WIREs Comput Mol Sci* **2012**, *2*, 242–253.
- [52] Ho, T.-S.; Rabitz, H. *J. Phys. Chem.* **1996**, *104*, 2584.
- [53] Castro-Palacio, J. C.; Nagy, T.; Bemish, R. J.; Meuwly, M. *J. Chem. Phys.* **2014**, *141*(16), 164319.
- [54] Johnson III, R. D. In *Abstracts of Papers of the American Chemical Society*, Vol. 219, pages U611–U611. Amer Chemical Soc 1155 16TH ST, NW, Washington, DC 20036 USA, 2000.
- [55] Verlet, L. *Phys. Rev.* **1967**, *159*(1), 98.
- [56] Liboff, R. L. *Introductory quantum mechanics*; Addison-Wesley, 2003.

- [57] Porter, R.; Raff, L.; Miller, W. *J. Chem. Phys.* **1975**, *63*(5), 2214–2218.
- [58] Daan, F.; Berend, S. *Understanding molecular simulation: From algorithms to applications*; Academic Press, 2002.
- [59] Meuwly, M.; Hutson, J. M. *J. Chem. Phys.* **1999**, *110*(17), 8338–8347.
- [60] Okabe, H. *Photochemistry of small molecules*; Wiley, New York, 1978.
- [61] Skouteris, D.; Castillo, J.; Manolopoulos, D. *ChemPhysChem* **2000**, *133*(1), 128–135.
- [62] Burkholder, J.; Abbatt, J.; Huie, R.; Kolb, C.; Orkin, V.; Wine, P.; Sander, S.; Barker, J.; Kurylo, M.; Wilmouth, D. Chemical kinetics and photochemical data for use in atmospheric studies: Evaluation number 18 Technical report, JPL Publication 15-10, Jet Propulsion Laboratory, Pasadena, **2015**.
- [63] Myatt, C.; Burt, E.; Ghrist, R.; Cornell, E.; Wieman, C. *Phys. Rev. Lett.* **1997**, *78*(4), 586.
- [64] Elioff, M. S.; Valentini, J. J.; Chandler, D. W. *Science* **2003**, *302*(5652), 1940–1943.
- [65] Schlemmer, S.; Kuhn, T.; Lescop, E.; Gerlich, D. *Int. J. Mass Spect.* **1999**, *185/186/187*, 589–602.
- [66] Grieman, J. C.; Hansen, J. T.; Moseley, J. *Chem. Phys. Lett.* **1982**, *85*, 53–56.
- [67] Candori, R.; Cavalli, S.; Pirani, F.; Volpi, A.; Cappelletti, D.; Tosi, P.; Bassi, D. *J. Chem. Phys.* **2001**, *115*, 8888–8898.
- [68] Teng, H. H.; Conway, D. *J. Chem. Phys.* **1973**, *59*(5), 2316–2323.
- [69] Schultz, R. H.; Armentrout, P. *Chem. Phys. Lett.* **1991**, *179*(5), 429–434.
- [70] Kato, S.; de Gouw, J. A.; Lin, C.-D.; Bierbaum, V. M.; Leone, S. R. *Chem. Phys. Lett.* **1996**, *256*(3), 305–311.
- [71] Germann, M.; Tong, X.; Willitsch, S. *Nat. Phys.* **2014**, *10*(11), 820–824.
- [72] Tong, X.; Nagy, T.; Reyes, J. Y.; Germann, M.; Meuwly, M.; Willitsch, S. *Chem. Phys. Lett.* **2012**, *547*, 1–8.
- [73] Castro-Palacio, J.; Bemish, R.; Meuwly, M. *J. Chem. Phys.* **2015**, *142*, 091104.
- [74] Ho, T.-S.; Hollebeek, T.; Rabitz, H.; Harding, L. B.; Schatz, G. C. *J. Chem. Phys.* **1996**, *105*(23), 10472–10486.
- [75] Czako, G.; Bowman, J. M. *Proceedings of the National Academy of Sciences* **2012**, *109*(21), 7997–8001.
- [76] de Oliveira-Filho, A. G.; Ornellas, F. R.; Bowman, J. M. *The journal of physical chemistry letters* **2014**, *5*(4), 706–712.
- [77] Sewell, T. D.; Thompson, D. L.; Gezelter, J. D.; Miller, W. H. *Chem. Phys. Lett.* **1992**, *193*(6), 512–517.

- [78] Varandas, A. *Chemical physics letters* **2007**, *439*(4), 386–392.
- [79] Bowman, J. M.; Gazdy, B.; Sun, Q. *The Journal of chemical physics* **1989**, *91*(5), 2859–2862.
- [80] Czako, G.; Kaledin, A. L.; Bowman, J. M. *Chemical Physics Letters* **2010**, *500*(4), 217–222.
- [81] Hollebeek, T.; Ho, T.-S.; Rabitz, H. *Annu. Rev. Phys. Chem.* **1999**, *50*, 537–570.
- [82] Hollebeek, T.; Ho, T.-K.; Rabitz, H. *J. Chem. Phys.* **1997**, *106*, 7223.
- [83] Dunning Jr, T. H. *J. Chem. Phys.* **1989**, *90*(2), 1007–1023.
- [84] Woon, D. E.; Dunning Jr, T. H. *The Journal of chemical physics* **1993**, *98*(2), 1358–1371.
- [85] Gaussian09 Revision A.02. Frisch, M. J.; Trucks, G. W.; Schlegel, H. B.; Scuseria, G. E.; Robb, M. A.; Cheeseman, J. R.; Scalmani, G.; Barone, V.; Mennucci, B.; Petersson, G. A.; Nakatsuji, H.; Caricato, M.; Li, X.; Hratchian, H. P.; Izmaylov, A. F.; Bloino, J.; Zheng, G.; Sonnenberg, J. L.; Hada, M.; Ehara, M.; Toyota, K.; Fukuda, R.; Hasegawa, J.; Ishida, M.; Nakajima, T.; Honda, Y.; Kitao, O.; Nakai, H.; Vreven, T.; Montgomery, Jr., J. A.; Peralta, J. E.; Ogliaro, F.; Bearpark, M.; Heyd, J. J.; Brothers, E.; Kudin, K. N.; Staroverov, V. N.; Kobayashi, R.; Normand, J.; Raghavachari, K.; Rendell, A.; Burant, J. C.; Iyengar, S. S.; Tomasi, J.; Cossi, M.; Rega, N.; Millam, J. M.; Klene, M.; Knox, J. E.; Cross, J. B.; Bakken, V.; Adamo, C.; Jaramillo, J.; Gomperts, R.; Stratmann, R. E.; Yazyev, O.; Austin, A. J.; Cammi, R.; Pomelli, C.; Ochterski, J. W.; Martin, R. L.; Morokuma, K.; Zakrzewski, V. G.; Voth, G. A.; Salvador, P.; Dannenberg, J. J.; Dapprich, S.; Daniels, A. D.; Farkas, .; Foresman, J. B.; Ortiz, J. V.; Cioslowski, J.; Fox, D. J.
- [86] Meuwly, M.; Hutson, J. M. *J. Chem. Phys.* **1999**, *110*(7), 3418 – 3427.
- [87] Singh, R. B.; Rai, D. K. *J. of Mol. Spec.* **1966**, *19*, 424 – 434.
- [88] Mähnert, J.; Baumgärtel, H.; Weitzel, K.-M. *J. Chem. Phys.* **1995**, *102*(1), 180–188.
- [89] Ho, T.; Rabitz, H. *J. Chem. Phys.* **1996**, *104*(7), 2584 – 2597.
- [90] Golub, G. H.; F., V. L. C. *Matrix Computations*; The Johns Hopkins University Press: Baltimore and London, 1983.
- [91] Soldan, P.; Hutson, J. M. *J. Chem. Phys.* **2000**, *112*(9), 4415 – 4416.
- [92] Xie, D.; Xu, C.; Ho, T.-K.; Rabitz, H.; G., L.; Lin, S. Y.; Guo, H. *J. Chem. Phys.* **2007**, *126*, 074315.
- [93] Yu, H.-G.; Nyman, G. *J. Chem. Phys.* **1999**, *111*(15), 6693–6704.
- [94] Brooks, B. R.; Brooks, III, C. L.; Mackerell, Jr., A. D.; Nilsson, L.; Petrella, R. J.; Roux, B.; Won, Y.; Archontis, G.; Bartels, C.; Boresch, S.; Caffisch, A.; Caves, L.; Cui, Q.; Dinner, A. R.; Feig, M.; Fischer, S.; Gao, J.; Hodoscek, M.; Im, W.; Kuczera, K.;

- Lazaridis, T.; Ma, J.; Ovchinnikov, V.; Paci, E.; Pastor, R. W.; Post, C. B.; Pu, J. Z.; Schaefer, M.; Tidor, B.; Venable, R. M.; Woodcock, H. L.; Wu, X.; Yang, W.; York, D. M.; Karplus, M. *J. Chem. Comp.* **2009**, *30*(10, SI), 1545–1614.
- [95] Abramowitz, M.; Stegun, I. A. *Handbook of mathematical functions: with formulas, graphs, and mathematical tables*, number 55; Courier Corporation, 1964.
- [96] Liboff, R. L. *Introductory Quantum Mechanics (4th ed.)*; Addison-Wesley, Massachusetts, 2003.
- [97] Peterson, J.; Le Padellec, A.; Danared, H.; Dunn, G.; Larsson, M.; Larson, A.; Peverall, R.; Strömholm, C.; Rosén, S.; Af Ugglas, M. *J. Chem. Phys.* **1998**, *108*(5), 1978–1988.
- [98] Colbourn, E.; Douglas, A. *Journal of Molecular Spectroscopy* **1977**, *65*(2), 332–333.
- [99] Andersson, S.; Barinovs, G.; Nyman, G. *The Astrophysical Journal* **2008**, *678*(2), 1042.
- [100] Eichelberger, B. R.; Snow, T. P.; Bierbaum, V. M. *Journal of the American Society for Mass Spectrometry* **2003**, *14*(5), 501–505.